

# Experimental Study of Fine Frequency Selection Techniques for Piezoelectric Aluminum Nitride Lamb Wave Resonators

*Ting-Ta Yen*



Electrical Engineering and Computer Sciences  
University of California at Berkeley

Technical Report No. UCB/EECS-2013-189

<http://www.eecs.berkeley.edu/Pubs/TechRpts/2013/EECS-2013-189.html>

December 1, 2013

Copyright © 2013, by the author(s).  
All rights reserved.

Permission to make digital or hard copies of all or part of this work for personal or classroom use is granted without fee provided that copies are not made or distributed for profit or commercial advantage and that copies bear this notice and the full citation on the first page. To copy otherwise, to republish, to post on servers or to redistribute to lists, requires prior specific permission.

---

**Experimental Study of Fine Frequency Selection Techniques  
for Piezoelectric Aluminum Nitride Lamb Wave Resonators**

by Ting-Ta Yen

---

**Research Project**

Submitted to the Department of Electrical Engineering and Computer Sciences,  
University of California at Berkeley, in partial satisfaction of the requirements for the  
degree of **Master of Science, Plan II.**

Approval for the Report and Comprehensive Examination:

**Committee:**

---

Professor Albert P. Pisano  
Research Advisor

---

(May 10, 2012)

\* \* \* \* \*

---

Professor Richard M. White  
Second Reader

---

(May 10, 2012)

**Experimental Study of Fine Frequency Selection Techniques  
for Piezoelectric Aluminum Nitride Lamb Wave Resonators**

Copyright © 2012

by

Ting-Ta Yen

## Abstract

### Experimental Study of Fine Frequency Selection Techniques for Piezoelectric Aluminum Nitride Lamb Wave Resonators

by

Ting-Ta Yen

Master of Science, Plan II in Electrical Engineering and Computer Sciences

University of California, Berkeley

Professor Albert P. Pisano, Chair

Strong demand for high- $Q$  resonators and filters in mobile wireless communication systems has initiated various research on radio frequency microelectromechanical systems (RF MEMS). Several CMOS-compatible RF MEMS resonator technologies, either electrostatic or piezoelectric, can provide multi-frequency operation on a single substrate and have the potential to realize a channel-select RF front-end architecture. However, utilizing a narrowband filter bank in such an architecture as the key component for frequency selection leads to a major challenge: fine frequency control. Depending upon the standard, it may entail the simultaneous fabrication of tens to hundreds of filters with 0.05 to 0.1% bandwidth, and spacing.

Aluminum nitride (AlN) Lamb wave resonators (LWRs) utilize piezoelectric transduction to ensure low motional resistance. The resonance frequency of a LWR is defined by interdigital transducer (IDT) pitch and is thus decoupled from the overall device dimensions. This fine frequency selection technique is enabled by adjusting the so-called AlN "overhang" dimension allowing control of relative frequency of Lamb wave resonators in an array to 0.1%. Experimental results suggest the center frequency of LWRs can be linearly adjusted by up to 5% with no significant effect on other resonator parameters including  $Q$ ,  $R_m$ ,  $C_0$ , and  $k_t^2$ . Closely and evenly spaced AlN Lamb wave resonators, without post-process trimming, demonstrate the potential to realize a pure mechanical, high performance, yet low power RF front-end system.

*To my parents*

# Contents

## 1 INTRODUCTION

<b>1.1 Motivation: An RF Channel-Select Architecture.....</b>	<b>1</b>
<b>1.2 Technical Challenges.....</b>	<b>3</b>
1.2.1 Multiple Frequencies .....	3
1.2.2 Impedance Match .....	3
1.2.3 Post-CMOS Compatibility .....	3
1.2.4 Fine Frequency Selection .....	4
<b>1.3 Existing Approaches.....</b>	<b>4</b>
1.3.1 Surface Acoustic Wave Devices.....	4
1.3.2 Bulk Acoustic Wave Devices .....	5
1.3.3 Contour-Mode Aluminum Nitride MEMS Devices .....	7
1.3.4 Electrostatic Vibrating MEMS Devices .....	8
1.3.5 Comparison .....	9
<b>1.4 Thesis Outline.....</b>	<b>10</b>

## 2 FUNDAMENTALS OF PIEZOELECTRIC TRANSDUCTION

<b>2.1 Piezoelectricity.....</b>	<b>11</b>
2.1.1 Piezoelectric Effect.....	11
2.1.2 Constitutive Equations .....	12
<b>2.2 Lamb Waves Characteristics .....</b>	<b>16</b>
<b>2.3 Material Properties of Aluminum Nitride.....</b>	<b>18</b>

## 3 FINE FREQUENCY SELECTION TECHNIQUES FOR ALN LAMB WAVE RESONATORS

<b>3.1 Resonator Basics.....</b>	<b>21</b>
3.1.1 Mason Model .....	22
3.1.2 One-Port Resonator Circuit Model .....	23
3.1.3 Quality Factor ( $Q$ ) .....	24
3.1.4 Electromechanical Coupling Coefficient ( $k_r^2$ ) .....	25

<b>3.2 Lamb Wave Resonator Design.....</b>	<b>26</b>
<b>3.3 Device Fabrication.....</b>	<b>27</b>
<b>3.4 Fine Frequency Selection Study for AlN Lamb Wave Resonators.....</b>	<b>30</b>
3.4.1 Adjusting Electrode Number, $n$ .....	32
3.4.2 Adjusting Device Length, $L$ .....	32
3.4.3 Adjusting Electrode Coverage, $\eta$ .....	33
3.4.4 Adjusting AlN Overhang, $OH$ .....	35
<b>4 CONCLUSION AND FUTURE WORK</b>	
<b>4.1 Conclusion .....</b>	<b>39</b>
<b>4.2 Future Research Directions .....</b>	<b>40</b>
4.2.1 Characterizing Thermal Stability.....	40
4.2.2 Investigating Energy Loss Mechanisms.....	40
4.2.3 Filter Synthesis with Different Couplings.....	41
4.2.4 Integration with IC.....	41
<b>BIBLIOGRAPHY .....</b>	<b>43</b>

# Chapter 1

---

## Introduction

Microelectromechanical systems (MEMS) benefiting from scaling have been researched and successfully commercialized in many fields of technology, especially sensors and actuators. Miniaturization in mechanical systems leads to higher speed, higher efficiency, higher degree of integration, lower power consumption, and usually lower cost. In recent decades, radio frequency microelectromechanical systems (RF MEMS) utilizing micro-mechanical structures vibrating at specific frequencies (from kilohertz up to gigahertz range) have replaced on-chip electrical RF devices to serve frequency control functions due to their high quality factor and performance. With quality factor  $10^3$ – $10^5$  times higher than their on-chip electrical counterparts, RF MEMS resonators offer promising building blocks to synthesize low-loss bandpass filters used in contemporary wireless communication systems.

This chapter will start by introducing a novel channel-select RF front-end architecture. The narrowband filter bank is the key component for the frequency selection function. Technical challenges of this architecture will be addressed, followed by short descriptions of existing technologies and their merits and demerits.

### 1.1 Motivation: An RF Channel-Select Architecture

In order to reduce power consumption and complexity of integration in next-generation communication systems, resonators and filters based on MEMS technology have been considered as direct replacements for off-chip passive components such as crystals, surface acoustic wave (SAW) filters, and inductors for bias and matching networks [1, 2]. Figure 1 presents block diagrams of possible receiver front-end architectures adapting MEMS resonator technology to realize a highly integrated system [2]. The direct conversion receiver architecture

[3, 4] uses minimum numbers of costly off-chip components including SAW band-select filters and quartz crystals used for the frequency control/reference purposes. Although this architecture has eliminated the need for IF filters and off-chip inductors, the use of RF low-noise amplifiers (LNAs) and transistor mixers increases the complexity of integrated circuits (IC) as well as their power consumption.

C. Nguyen *et al.* employed the advantages of high- $Q$  MEMS resonator technology to eliminate the need for RF LNAs and transistor mixers, and proposed a channel-select RF front-end architecture [2, 5]. The key feature of this architecture is the use of a multitude of closely spaced narrowband filters, *i.e.*, filter bank, paired with low loss switches to fulfill the frequency selection function. Due to the elimination of LNAs and mixers, this channel-select architecture significantly simplifies the circuits further down the receiver path and thereby reduces the power consumption while increasing capabilities of the whole system [1].

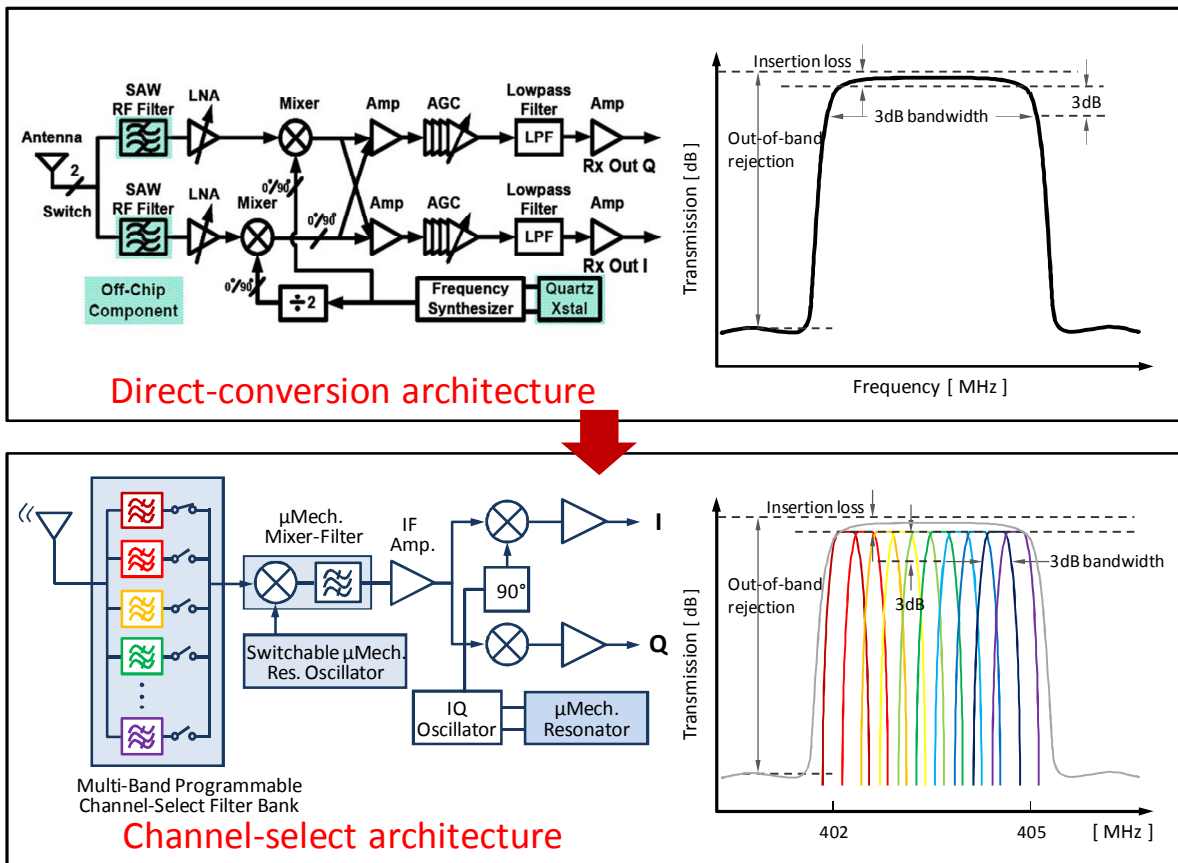


Figure 1.1 Two RF receiver front-end architectures via the use of MEMS resonators and filters [2]. Due to the elimination of LNAs and mixers, the channel-select architecture significantly simplifies the circuits further down the receiver path and thus effectively reduces the power consumption.

## 1.2 Technical Challenges

This multi-band RF front-end requires the ability to fabricate closely spaced narrowband RF filters. Several MEMS resonator technologies, either electrostatic [1, 6] or piezoelectric [7, 8], could provide multi-band operation on a single silicon substrate and have the potential to implement this channel-select architecture. The technical challenges are discussed in this section.

### 1.2.1 Multiple Frequencies

The emerging demands of highly-integrated wireless communication systems have raised the needs for monolithic integration of various passive frequency control elements on a single substrate. For example, most current CDMA/GSM cellular phones, requiring a dozen or even more bandpass filters from the intermediate frequency (IF) to the Bluetooth band, use off-chip quartz, SAW devices, or thin-film bulk acoustic resonator (FBAR) components for the frequency selection purpose. The proposed channel-select architecture will require the ability to fabricate 10 to 100 closely spaced narrowband RF filters which reinforces the necessity to integrate all filters on a single die.

### 1.2.2 Impedance Match

Presently, most microwave hardware is specified to run in the 50-ohm characteristic impedance system due to historical reasons [9, 10]. In dealing with AC signals, the maximum power transfer from the source to the load occurs when the load impedance ( $Z_L$ ) is equal to the complex conjugate of the source impedance ( $Z_S$ ). Impedance mismatch brings in reflections between interconnected circuit elements which impede power transfer and therefore affect system performance. For filter applications, large motional resistance of a resonator translates into large insertion losses or the need for bulky matching elements which make them difficult to be integrated with existing 50-ohm systems.

### 1.2.3 Post-CMOS Compatibility

Thermal budget is the total amount of thermal energy transferred to the wafer during a given elevated temperature fabrication process. To prevent redistribution of dopants and damage of CMOS electronics with aluminum or copper metallization, post-CMOS MEMS process temperature should be limited to a maximum of 450°C [11]. To achieve the highest order of integration, candidate technologies should adapt only CMOS-compatible structural materials. The system performance could also benefit from the replacement of discrete crystal/filter components with highly-integrated low-thermal-budget thin-film MEMS solutions by reducing parasitic noises and packaging size.

## 1.2.4 Fine Frequency Selection

To correct deviations of operating frequency, post-process trimming is usually necessary for commercialized products. Depending upon the standard, the channel-select architecture may entail the simultaneous fabrication of tens to hundreds of narrowband filters with 0.05 to 0.1% bandwidth and 0.05 to 0.1% center frequency spacing. Mass loading and laser trimming are two commonly used methods for post-process fine frequency tuning; however they are costly and impractical for a filter bank with more than ten filters. It would therefore be advantageous to develop fine frequency selection techniques or active trimming techniques to define the relative center frequency of each resonator in an array.

## 1.3 Existing Approaches

The discovery of piezoelectricity by the Curie brothers in 1880 led to the emerging research and applications of electro-acoustic (EA) devices. By imposing different boundary conditions to the equation of motion, different types of acoustic waves can be obtained. They can be roughly categorized into: surface acoustic waves (SAW), bulk acoustic waves (BAW), and plate acoustic waves (PAW). Except for the piezoelectric transduction, electrostatic MEMS resonators made of poly-silicon, poly silicon-germanium, or metals also provide promising solutions. This section will give a short introduction to four current resonator technologies. A short comparison based on previously mentioned technical challenges will also be presented.

### 1.3.1 Surface Acoustic Wave Devices

In 1885, Lord Rayleigh first described the acoustic waves with longitudinal and vertical shear components and named them surface acoustic waves (SAW) [12]. These discoveries remained scientific research topics until the breakthrough invention of using interdigital transducer (IDT) on piezoelectric substrates by R. White and F. Voltmer in 1965 [13]. Since then, this technology has dominated the market for decades.

Figure 1.2 shows two commonly used SAW resonator topologies and the laser interferometer images of the propagating surface acoustic waves. This type of acoustic wave only propagates near the surface of a semi-infinite solid and the amplitude decays exponentially with depth into the substrate. They can be confined by reflector structures or gratings at either end of the IDT array and form standing waves. Besides, SAW can couple with any media in contact with the surface and is therefore widely used in non-destructive defect testing. One of the earliest successful applications was the intermediate frequency (IF) bandpass filter for television

receivers [14]. Single crystalline quartz, lithium niobate ( $\text{LiNbO}_3$ ), and lithium tantalate ( $\text{LiTaO}_3$ ) are commonly used substrate materials for SAW devices.

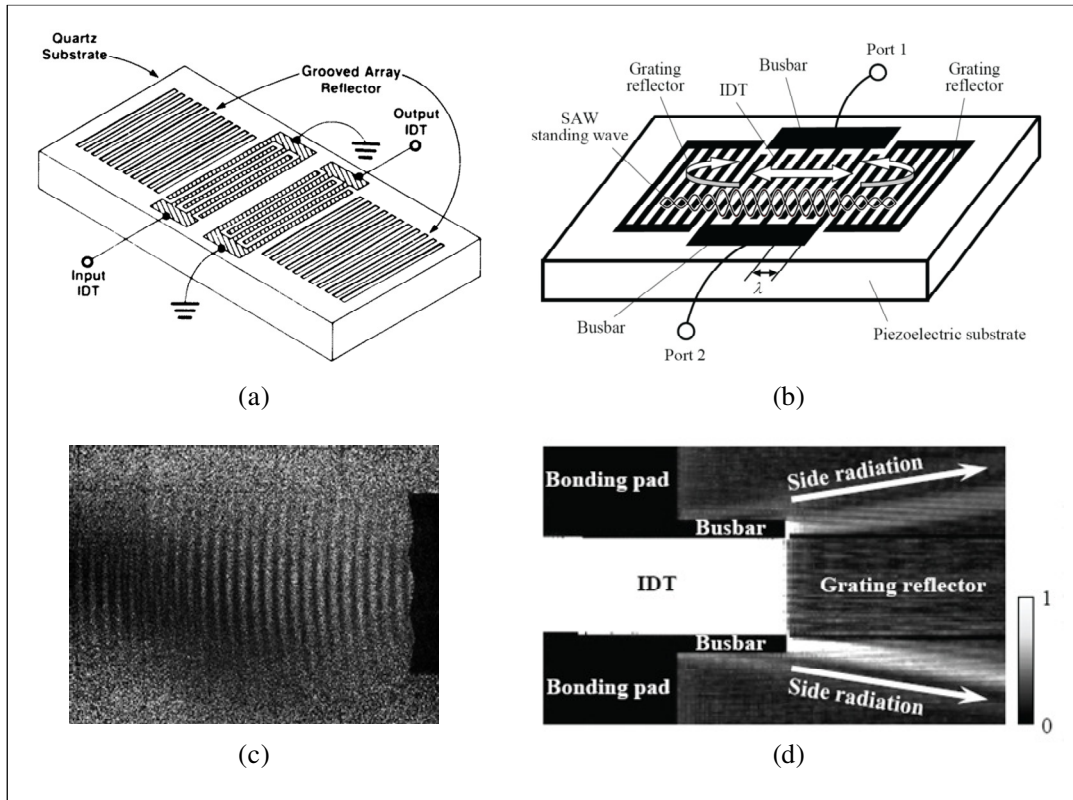


Figure 1.2 SAW resonators and the laser interferometer images: (a) and (b) are two commonly used topologies for SAW resonators [15]; (c) shows a laser interferometer image of a SAW propagating on an aluminum surface [16]; (d) corresponds to the side acoustic radiation of a shear horizontal leaky SAW (SH-LSAW) by using the polarization detection method [15].

In a given substrate, the frequency of SAW devices is determined by the IDT electrode pitch which in turn is limited by the resolution of the lithography tool. For higher frequency applications, substrates with higher acoustic velocity are necessary. H. Nakahata and G. Iriarte *et al.* have demonstrated SAW devices with phase velocity exceeding 10,000 m/s using AlN/poly-diamond composite layers [17, 18].

### 1.3.2 Bulk Acoustic Wave Devices

Among all types of acoustic waves, the bulk acoustic wave (BAW) is the first one to have practical applications due to its simple generating/detecting structure. P. Langevin first utilized the BAW in a steel-quartz-steel transducer for a submarine sonar system during World War I. Since then, quartz has been of primary importance in both frequency control and sensor applications due to its superior low acoustic losses and excellent temperature stability. The

quartz crystal microbalance (QCM) is another widely used sensor utilizing BAW for the detection of mass loading from atomic and molecular species.

In the microwave region, the traditional EA technologies use bulk single-crystalline piezoelectric substrates. Although having excellent performance and temperature stability, these bulk materials are not compatible with existing CMOS processing and are difficult to scale to higher frequency applications. The successful synthesis of high quality zinc oxide (ZnO) thin film on silicon by reactive sputter deposition initiated thin-film EA technologies. Solidly mounted resonators (SMR) and thin-film bulk acoustic resonators (FBAR) are two commercialized technologies utilizing BAW in piezoelectric thin films. Figure 1.3 describes these two technologies.

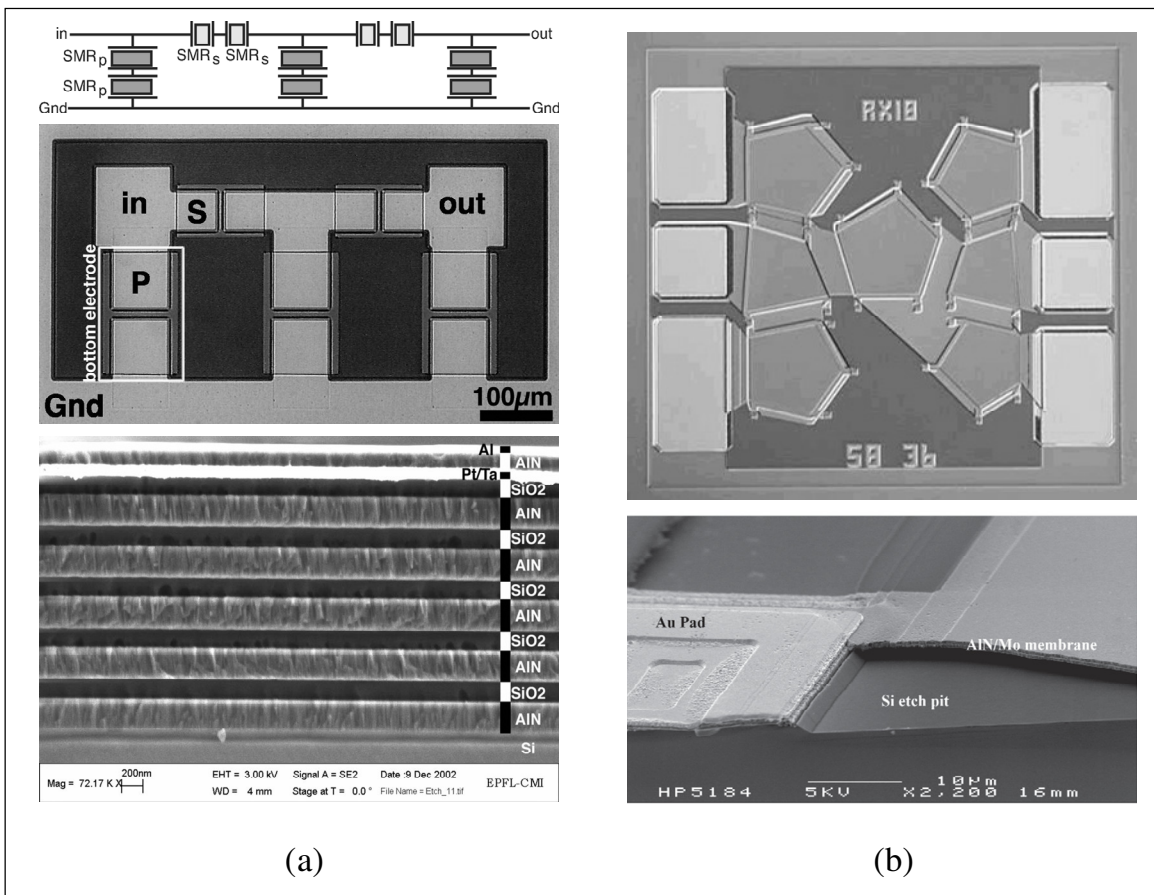


Figure 1.3 Two commercially available bulk acoustic wave resonator technologies: (a) Top view of a 2-stage  $\pi$  ladder filter and the cross-section view of five  $\lambda/4$ -reflector stacks of the SMR [19]; (b) A top view of a receiver (Rx) chip used in a PCS duplexer composed of three series and four shunt FBARs [20] and the side view of the AlN membrane stretching over a micromachined silicon pit [21].

For SMR technology, the piezoelectric thin film is deposited on a Bragg reflector stack which consists of alternating pairs of high and low acoustic impedance materials [22]. The operation is based on transducing standing bulk acoustic waves across the thickness direction of an acoustically isolated piezoelectric thin film. Those layers in the Bragg reflector are of quarter wavelength thickness of the desired frequency to reflect most of the acoustic energy leaking to the substrate. Though this non-free-standing structure is very resistant to shock damage, the precise thickness control dramatically increases the fabrication costs. On the other hand, the FBAR structure is a released and free-standing piezoelectric membrane which is also sandwiched between top and bottom electrodes. FBAR resonators utilize the (0002)-oriented AlN films since this direction exhibits the highest piezoelectric coefficients. The boundaries between the piezoelectric layer and the air gap enable a high reflectance of the acoustic waves and high  $Q$  values. Common applications using FBAR technology are RF filters and duplexers at 1.9 GHz for cellular phone applications.

### 1.3.3 Contour-Mode Aluminum Nitride MEMS Devices

AlN contour-mode resonator technology has been developed in Berkeley Micromechanical Analysis and Design (BMAD) research group since 2002. Similar to FBAR, these resonators consist of a piezoelectric AlN structure layer sandwiched between top and bottom electrodes, and normally anchored with quarter-wavelength long tethers to the surrounding materials. An isotropic xenon difluoride ( $\text{XeF}_2$ ) dry release step is applied to remove the silicon substrate beneath each resonator to form the acoustic isolation. Figure 1.4 shows some of these contour-mode resonators developed in BSAC. The in-plane device dimensions determine the resonance frequencies of these devices: device A is a width-extensional mode rectangular plate and the resonance frequency is defined by its width dimension, whereas device E adapts a circular ring topology and sets the frequency by its inner- and outer-radius ratio.

On the other hand, the motional resistance of a contour-mode resonator is in reciprocal proportion to the effective transduction area. A resonator operating at VHF (30 – 300MHz) or IF bands has a typical motional resistance value less than 100  $\Omega$  and the quality factor  $Q$  above 1,000 (measured in the atmosphere) [8, 23-26]. Decreasing the lateral dimensions corresponding to the standing wavelength for higher frequency applications results in increasing the motional resistance and thus poses a design dilemma.

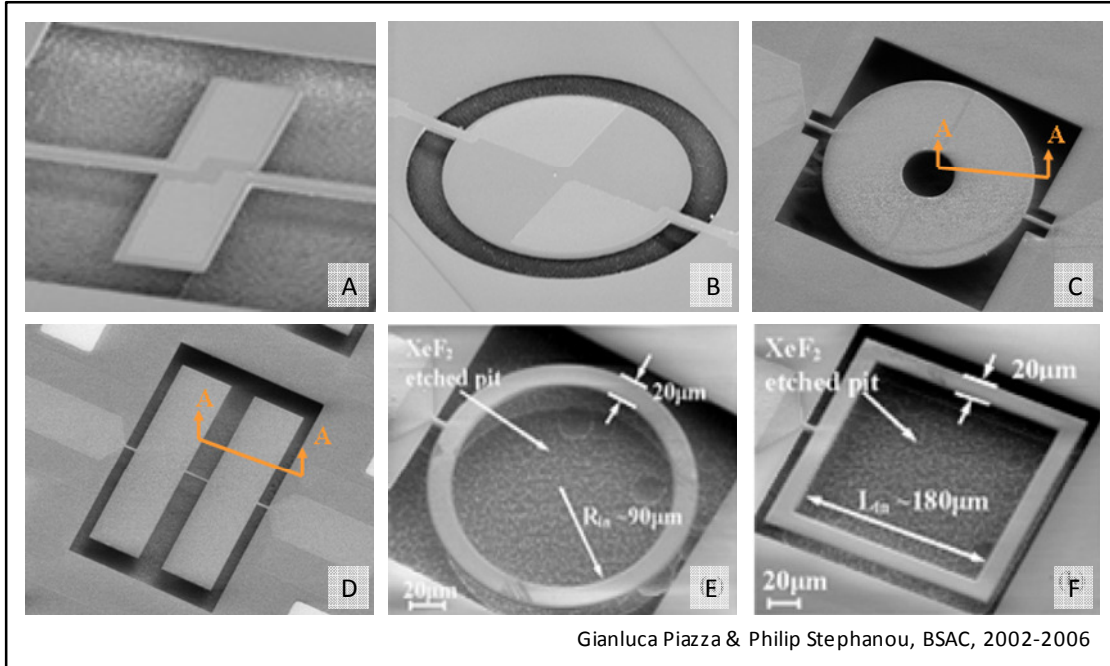


Figure 1.4 AlN contour-mode resonators with different topologies: A is a two-port width-extensional mode rectangular resonator; B is an AlN disk excited in a wineglass contour mode [23]; C is a dual mode annular resonator [24]; D shows two rectangular plate resonators mechanically coupled through a  $\lambda/4$  coupling beam [25]; E and F are single-support circular- and rectangular-shaped ring resonators [26].

### 1.3.4 Electrostatic Vibrating MEMS Devices

Electrostatic MEMS resonators using single-crystal silicon, poly-silicon (poly-Si), or polycrystalline silicon-germanium (poly-SiGe) as device layers have been studied since the 1990s. Most of these devices are fabricated using surface micromachining processes. The transduction is based on introducing electrostatic force across a sub-micron air-gap [5] or a dielectric-filled gap [27-29], and then transducing acoustic waves across the acoustically isolated disks or plates.

The resonance frequency is determined by the lateral dimensions and can be set at the layout level. These electrostatic resonators typically have  $Q$  greater than 10,000 and are excellent solutions to replace quartz oscillator crystals in reference clock circuits [30, 31]. However the small electromechanical coupling and high motional impedance make their interface with 50-ohm systems very difficult and limit the applications for RF filters.

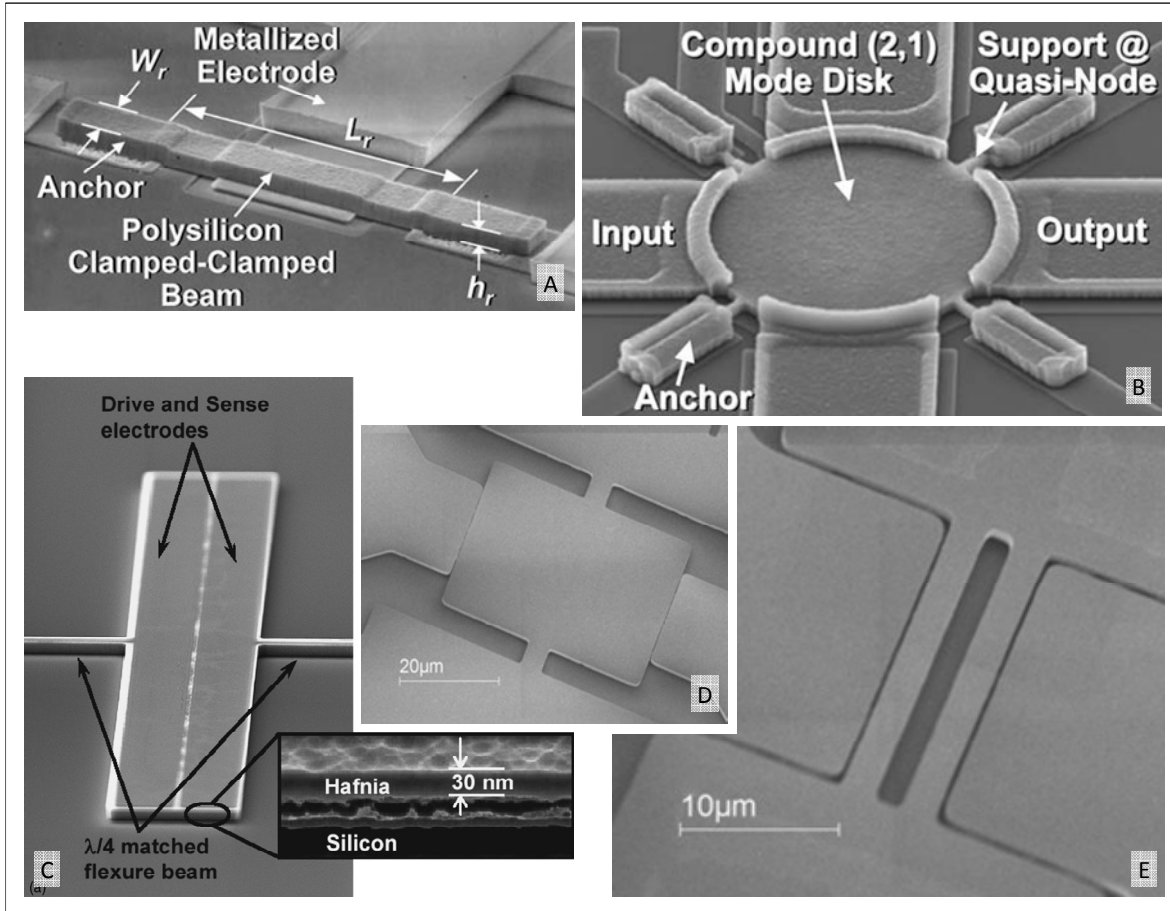


Figure 1.5 Electrostatic resonators: device A is a poly-Si clamped-clamped beam flexural-mode resonator [32] and B is a wine-glass disk resonator [33]; device C is a hafnium dioxide-on-silicon bar shear mode resonator [6]; device D and E are a bulk-longitudinal resonator and a double-ended tuning fork (DETF) resonator both made of poly-SiGe [34].

### 1.3.5 Comparison

The SAW devices are one of the most mature EA technologies and have been dominated the market for decades owing to their simple fabrication process (usually less than two masks). The piezoelectric transduction ensures high electromechanical coupling and low motional resistance. Certain cuts of quartz even have extremely good thermal stability and is widely used for timing references. Although some research groups have started investigating the fabrication of SAW devices on piezoelectric thin films deposited on silicon wafers [35, 36], single crystalline substrates currently used in conventional SAW devices are still exotic and incompatible with current CMOS process and have precluded the monolithic integration with circuits. The low phase velocity of SAW also requires the use of a high resolution lithography tool for high frequency applications.

Although having the highest acoustic velocity and the lowest motional resistance among all piezoelectric resonator technologies, the FBAR or SMR devices define the resonance frequency by the thin film thickness and cannot fulfill the needs for building multitude channels on a single chip without post-process trimming. Besides, the high electromechanical coupling of BAW devices enables the wide bandwidth applications such as duplexers and band select filters. However, this feature also indicates the difficulty to synthesize narrowband filter banks proposed here.

AlN contour-mode MEMS resonator technology sets the operation frequencies by in-plane dimensions and enables building multiple frequency devices on a single chip. As with other piezoelectric transduction AE devices, AlN contour-mode resonators typically have a motional resistance less than  $200\ \Omega$  and can be designed close to  $50\ \Omega$  for easy impedance matching. High quality AlN thin film can be synthesized by AC reactive sputtering at  $350^\circ\text{C}$ , a low-thermal-budget, post-CMOS-compatible deposition process. Although with very high  $Q$  at IF band, it is impractical to adapt this topology for UHF (300 MHz – 3 GHz) applications and fine frequency selection with 0.1% relative frequency shifting by each channel.

The electrostatic resonators having extremely high  $Q$  are very suitable as replacements of oscillator crystals. However, devices with high motional resistance are very difficult to match to 50-ohm circuits or antennas by using on-chip matching networks which only provide a termination impedance of the order of 1 k $\Omega$ . Besides, in order to avoid damaging CMOS electronics with metal interconnects, the post-CMOS MEMS process temperatures is recommended to be limited to a maximum of  $450^\circ\text{C}$ . This constraint rules out the conventional poly-Si as a candidate structural material for post-CMOS integrated MEMS [11]. Low temperature processes such as poly-SiGe or metal processes are alternative solutions for modular integration of MEMS with electronics due to the much lower deposition temperature.

## 1.4 Thesis Outline

This research thesis is laid out in four chapters. Chapter 1 has presented the research motivation, technical challenges, and existing solutions. Chapter 2 will provide the fundamentals of piezoelectric transduction, material properties of aluminum nitride, and characteristics of Lamb waves propagating in a piezoelectric thin film. Resonator basics, design, and the fabrication process will be discussed in Chapter 3. Experimental study of four fine frequency selection techniques by adjusting electrode number  $n$ , device length  $L$ , electrode coverage  $\eta$ , and the overhang  $OH$  will also be demonstrated in this chapter. Chapter 4 will conclude the whole work and point out the potential research directions.

# Chapter 2

---

## Fundamentals of Piezoelectric Transduction

Piezoelectricity is a well studied and widely used physical effect that has its name derived from the Greek word *piezein*, meaning "to press". Crystals which acquire charges when compressed, twisted, or distorted are said to be piezoelectric. This effect is an inherent material property in crystals having no center of symmetry. In this chapter, fundamental piezoelectric transduction will be discussed. It will start with basic governing equations of piezoelectric transduction, and then discuss the characteristics of Lamb waves propagating in the AlN thin film. Electrical and piezoelectric material properties of AlN will also be discussed at the end of the chapter.

### 2.1 Piezoelectricity

#### 2.1.1 Piezoelectric Effect

Piezoelectricity is described as the formation of the electric polarization or electric charges induced by a mechanical strain. Conversely, a mechanical deformation is produced when an electric field is applied to a piezoelectric substance. This is an inherent property of a material that has a non-symmetrical crystallographic structure with respect to a point (lacks a center of symmetry) and provides a convenient transduction between electrical and mechanical oscillations. Crystals with a center of symmetry, such as cubic crystals, are not piezoelectric because the net electric dipole within the primitive unit cell is always zero, no matter how the structure deforms.

The physical origin of piezoelectricity comes from the charge asymmetry within the primitive unit cell which results in the formation of a net electric dipole. The polar axis is an

imaginary line that pointing through the center of the negative and positive charges in the dipole. In a monocrystal, the polar axes of all the dipoles lie in one direction. This crystal is called symmetrical since no matter how the crystal is cut, the polar axes will remain in the same direction as the original. A polycrystal is called asymmetrical since within which the polar axes are pointing randomly in different regions. Adding up these individual dipoles over the entire crystal gives a net polarization and an effective electric field within the material.

A typical experimental configuration is shown in Figure 2.1. When a voltage is applied across along one of the major axes, the  $e_{ii}$  term piezoelectric coefficient maps the electric field to the induced stress along that direction, while the  $e_{ij}$  term maps the electric field to the induced stress along orthogonal axes.

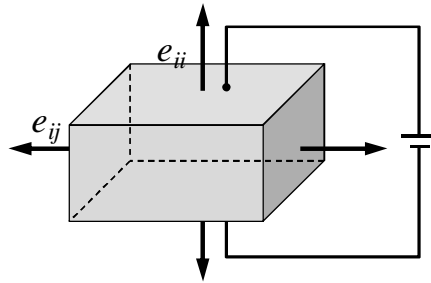


Figure 2.1 Qualitative determination of piezoelectric constants:  $e_{ii}$  maps the electric field to the stress along the same direction, and  $e_{ij}$  maps the electric field to stress along orthogonal axes.

If an oscillating electric field is applied to a piezoelectric substrate, the substrate will respond with mechanical vibrations and produce mechanical waves. Distortions of these crystals restore the system to equilibrium through internal elastic forces. The potential energy restored from particle distortions combine with particle inertia produces an oscillation. These motions are on the order of nanometers and have been used in the precise control of scanning tunneling microscopes (STM) tips.

### 2.1.2 Constitutive Equations

For a linearly elastic media, the well-known Hooke's Law is used to describe the relation of stress  $T$  and strain  $S$  as

$$T = cS \quad \text{or} \quad S = sT \quad (2.1)$$

where  $c$  is the elastic stiffness constant and  $s$  is the elastic compliance constant. Similarly, in the electrical domain, Equation 2.2 relates the electric charge density displacement  $D$  and electric field  $E$ ,

$$D = \epsilon E \quad \text{or} \quad E = \beta D \quad (2.2)$$

Piezoelectricity is the combined effect of the Hooke's Law and the electrical behavior of the material. Depending on the variable choice (mechanical stress  $T$ , mechanical strain  $S$ , electrical field  $E$ , and electrical displacement  $D$ ), Equation 2.3 represents the constitutive relations of piezoelectricity:

$$\begin{aligned} & \begin{cases} T = c^D S - hD \\ E = \beta^S D - hS \end{cases} & h\text{-form} \\ & \begin{cases} S = s^E T + dE \\ D = \epsilon^T E + dT \end{cases} & d\text{-form} \\ & \begin{cases} S = s^D T + gD \\ E = \beta^T D - gT \end{cases} & g\text{-form} \\ & \begin{cases} T = c^E S - eE \\ D = \epsilon^S E + eS \end{cases} & e\text{-form} \end{aligned} \quad (2.3)$$

These four sets of equations represent the same piezoelectric relations but are expressed with different forms named after the piezoelectric coefficients coupling the electrical and mechanical domains. Piezoelectric coefficients  $h$ ,  $d$ ,  $g$ , and  $e$  can be converted into each other. Equation 2.4 relates these four piezoelectric coefficients [37]:

$$\begin{aligned} h_{ij} &= -(\partial E_i / \partial S_j)^D = -(\partial T_j / \partial D_i)^S \\ d_{ij} &= (\partial D_i / \partial T_j)^E = (\partial S_j / \partial E_i)^T \\ g_{ij} &= -(\partial E_i / \partial T_j)^D = (\partial S_j / \partial D_i)^T \\ e_{ij} &= (\partial D_i / \partial S_j)^E = -(\partial T_j / \partial E_i)^S \end{aligned} \quad (2.4)$$

The first set of four terms correspond to the direct piezoelectric effect and the second set of four terms describe the converse piezoelectric effect.

The  $e$ -form is used to describe the piezoelectric phenomenon throughout this thesis,

$$\begin{cases} T_{ij} = c_{ijkl}^E S_{kl} - e_{kij}^T E_k \\ D_i = \epsilon_{ik}^S E_k + e_{ikl} S_{kl} \end{cases} \quad (2.5)$$

where the two equations are coupled through the stress-charge piezoelectric tensor  $e$ . The superscripts  $E$  and  $S$  in the stiffness constant and dielectric constant denote that they have been measured at constant electric field and constant strain, respectively; whereas the superscript  $T$  in the piezoelectric coefficient represents the transpose of the tensor  $e$ . The full expression of Equation 2.5 is shown below:

$$\begin{bmatrix} T_1 \\ T_2 \\ T_3 \\ T_4 \\ T_5 \\ T_6 \end{bmatrix} = \begin{bmatrix} c_{11} & c_{12} & c_{13} & c_{14} & c_{15} & c_{16} \\ & c_{22} & c_{23} & c_{24} & c_{25} & c_{26} \\ & & c_{33} & c_{34} & c_{35} & c_{36} \\ & & & c_{44} & c_{45} & c_{46} \\ & & & & c_{55} & c_{56} \\ & & & & & c_{66} \end{bmatrix} \begin{bmatrix} S_1 \\ S_2 \\ S_3 \\ S_4 \\ S_5 \\ S_6 \end{bmatrix} - \begin{bmatrix} e_{11} & e_{21} & e_{31} \\ e_{12} & e_{22} & e_{32} \\ e_{13} & e_{23} & e_{33} \\ e_{14} & e_{24} & e_{34} \\ e_{15} & e_{25} & e_{35} \\ e_{16} & e_{26} & e_{36} \end{bmatrix} \begin{bmatrix} E_1 \\ E_2 \\ E_3 \end{bmatrix} \quad (2.6)$$

$$\begin{bmatrix} D_1 \\ D_2 \\ D_3 \end{bmatrix} = \begin{bmatrix} \epsilon_1 & \epsilon_6 & \epsilon_5 \\ & \epsilon_2 & \epsilon_4 \\ & & \epsilon_3 \end{bmatrix} \begin{bmatrix} E_1 \\ E_2 \\ E_3 \end{bmatrix} + \begin{bmatrix} e_{11} & e_{12} & e_{13} & e_{14} & e_{15} & e_{16} \\ e_{21} & e_{22} & e_{23} & e_{24} & e_{25} & e_{26} \\ e_{31} & e_{32} & e_{33} & e_{34} & e_{35} & e_{36} \end{bmatrix} \begin{bmatrix} S_1 \\ S_2 \\ S_3 \\ S_4 \\ S_5 \\ S_6 \end{bmatrix}$$

For a piezoelectric medium with hexagonal symmetry (point group 6mm) such as c-oriented columnar-growth AlN or ZnO, the constitutive relation can be further simplified in Equation 2.7 as

$$\begin{bmatrix} T_1 \\ T_2 \\ T_3 \\ T_4 \\ T_5 \\ T_6 \end{bmatrix} = \begin{bmatrix} c_{11} & c_{12} & c_{13} & 0 & 0 & 0 \\ & c_{11} & c_{12} & 0 & 0 & 0 \\ & & c_{33} & 0 & 0 & 0 \\ & & & c_{44} & 0 & 0 \\ & & & & c_{44} & 0 \\ & & & & & c_{66} \end{bmatrix} \begin{bmatrix} S_1 \\ S_2 \\ S_3 \\ S_4 \\ S_5 \\ S_6 \end{bmatrix} - \begin{bmatrix} 0 & 0 & e_{31} \\ 0 & 0 & e_{31} \\ 0 & 0 & e_{33} \\ 0 & e_{15} & 0 \\ e_{15} & 0 & 0 \\ 0 & 0 & 0 \end{bmatrix} \begin{bmatrix} E_1 \\ E_2 \\ E_3 \end{bmatrix}, \quad c_{66} = \frac{c_{11} - c_{12}}{2} \quad (2.7)$$

$$\begin{bmatrix} D_1 \\ D_2 \\ D_3 \end{bmatrix} = \begin{bmatrix} \epsilon_1 & 0 & 0 \\ & \epsilon_1 & 0 \\ & & \epsilon_3 \end{bmatrix} \begin{bmatrix} E_1 \\ E_2 \\ E_3 \end{bmatrix} + \begin{bmatrix} 0 & 0 & 0 & 0 & e_{15} & 0 \\ 0 & 0 & 0 & e_{15} & 0 & 0 \\ e_{31} & e_{31} & e_{33} & 0 & 0 & 0 \end{bmatrix} \begin{bmatrix} S_1 \\ S_2 \\ S_3 \\ S_4 \\ S_5 \\ S_6 \end{bmatrix}$$

There are 10 non-zero independent coefficients:  $c_{11}$ ,  $c_{12}$ ,  $c_{13}$ ,  $c_{33}$ ,  $c_{44}$ ,  $e_{15}$ ,  $e_{31}$ ,  $e_{33}$ ,  $\varepsilon_1(\varepsilon_{11})$ ,  $\varepsilon_3(\varepsilon_{33})$ . For example, the  $e_{31}$  term piezoelectric coefficient maps the thickness electric field to contour stress in the mechanical constitutive equation (or maps the contour strain to thickness charge flux in the electrical constitutive equation).

It is worth mentioning that the strain  $S$  and stress  $T$  are second rank tensors, but possess only six independent terms. Therefore they are expressed as  $6 \times 1$  column vectors in Equation 2.7 for convenience. For example, these six independent strain components can be written as the product of a differential operator matrix on a vector as in Equation 2.8 [38],

$$S = \begin{bmatrix} S_1 \\ S_2 \\ S_3 \\ S_4 \\ S_5 \\ S_6 \end{bmatrix} = \begin{bmatrix} \frac{\partial}{\partial x} & 0 & 0 \\ 0 & \frac{\partial}{\partial y} & 0 \\ 0 & 0 & \frac{\partial}{\partial z} \\ 0 & \frac{\partial}{\partial z} & \frac{\partial}{\partial y} \\ \frac{\partial}{\partial z} & 0 & \frac{\partial}{\partial x} \\ \frac{\partial}{\partial y} & \frac{\partial}{\partial x} & 0 \end{bmatrix} \cdot \begin{bmatrix} u_x \\ u_y \\ u_z \end{bmatrix} \quad (2.8)$$

The in-plane equivalent Young's modulus and Poisson's ratio of crystals with hexagonal symmetry can also be expressed in terms of the stiffness coefficients by Equation 2.9 and Equation 2.10 respectively:

$$E_1 = \frac{2c_{13}^2c_{12} - 2c_{13}^2c_{11} + c_{11}^2c_{33} - c_{33}c_{12}^2}{c_{11}c_{33} - c_{13}^2} \quad (2.9)$$

$$\nu_{12} = \frac{c_{12}c_{33} - c_{13}^2}{c_{11}c_{33} - c_{13}^2} \quad (2.10)$$

Equation 2.11 lists the stiffness matrix, piezoelectric stress matrix, and dielectric matrix of AlN thin film used in this thesis [39]:

$$\begin{aligned}
[c] &= \begin{bmatrix} 3.45 & 1.25 & 1.20 & 0 & 0 & 0 \\ 1.25 & 3.45 & 1.20 & 0 & 0 & 0 \\ 1.20 & 1.20 & 3.95 & 0 & 0 & 0 \\ 0 & 0 & 0 & 1.18 & 0 & 0 \\ 0 & 0 & 0 & 0 & 1.18 & 0 \\ 0 & 0 & 0 & 0 & 0 & 1.10 \end{bmatrix} (10^{11} N/m^2) \\
[e] &= \begin{bmatrix} 0 & 0 & 0 & 0 & -0.48 & 0 \\ 0 & 0 & 0 & -0.48 & 0 & 0 \\ -0.58 & -0.58 & 1.55 & 0 & 0 & 0 \end{bmatrix} (C/m^2) \\
[\varepsilon] &= \begin{bmatrix} 8.0 & 0 & 0 \\ 0 & 8.0 & 0 \\ 0 & 0 & 9.5 \end{bmatrix} (10^{-11} F/m)
\end{aligned} \tag{2.11}$$

## 2.2 Lamb Waves Characteristics

By imposing different boundary conditions to the equation of motion, different types of acoustic waves can be obtained in a substrate or in a thin film. The BAW and SAW devices have been studied for decades and successfully implemented in wireless communication applications. For a given substrate, the resonance frequency for SAW devices is determined by the IDT electrode pitches and in turn is limited by the lithography resolution. On the other hand, the resonance frequency for BAW devices is defined by the thin film thickness and allows very restricted fabrication tolerances. With the drive towards higher frequency applications, acoustic waves with high phase velocity (symmetric Lamb wave for example) attracted research attentions and triggered thin film electro-acoustic technologies, which occurred after the successful synthesis of high-quality zinc oxide (ZnO) thin films on silicon by reactive sputter deposition. This section discusses the characteristics of Lamb waves propagating in a thin film, and explains the reasons we employ the AlN Lamb wave technology.

When surface acoustic waves are guided laterally into a thin plate, they are referred to as Rayleigh–Lamb waves or Lamb waves [40]. The Lamb waves only exist in thin plates with thickness comparable or smaller than the acoustic wavelength and cause a wave-guide effect. Depending on the phase difference of particle displacements between top and bottom surfaces, Lamb waves are divided into symmetric and anti-symmetric modes as illustrated in Figure 2.2. The anti-symmetric modes are referred to as higher-order flexural modes in some literature. For

sufficiently thin plates, only the lowest order symmetric mode ( $S_0$ ) and anti-symmetric mode ( $A_0$ ) are observed [41].



Figure 2.2 Symmetric and anti-symmetric Lamb wave modes.

Figure 2.3 plots the phase velocities of the  $S_0$  and  $A_0$  modes as a function of normalized plate thickness ( $1 \mu\text{m}$ ). Compared with the  $A_0$  mode, the  $S_0$  mode shows a phase velocity over  $9800 \text{ m/s}$  and is therefore suitable for the fabrication of high-frequency devices. The dispersive curves in Figure 2.3 also indicate that the phase velocities of the Lamb waves are not solely determined by the material constants but also by the ratio of the thickness of the thin film to the wavelength. More importantly, the flat dispersion of  $S_0$  mode betokens the insensitivity of the  $S_0$  phase velocity to the AlN thin film thickness. In other words, the use of an  $S_0$  mode Lamb wave instead of BAW helps to improve the fabrication tolerance towards AlN thickness variations.

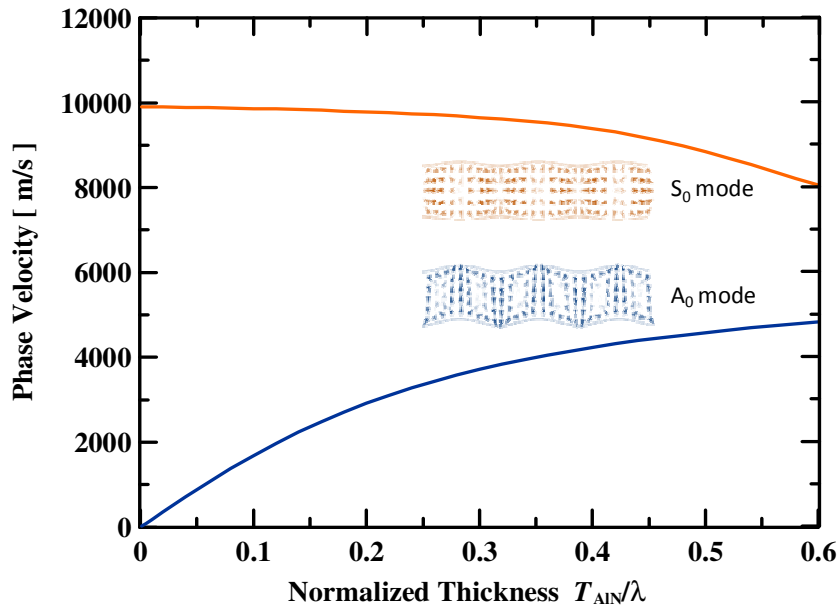


Figure 2.3 Phase velocity of  $S_0$  and  $A_0$  modes versus normalized AlN plate thickness ( $1 \mu\text{m}$ ).

Generally, a thin plate can support a number of Lamb waves depending on the ratio of the plate thickness to the wavelength and also the strength of electromechanical coupling. Inspired from SAW devices, Lamb wave resonators also utilize interdigital transducer (IDT) electrodes to

excite Lamb waves propagating in the piezoelectric thin films. For a given thickness, the resonance frequency is determined by the IDT electrode pitch and is thus effectively decoupled from the overall device dimensions.

To locally confine Lamb waves, Bjurstöm, Yantchev, and Katardjiev [7] use distributed Bragg reflectors formed by quarter-wavelength metal strips and periodically placed on each side of the transducer as shown in Figure 2.4. In this thesis, all Lamb wave resonators adapt the edge type reflectors to confine Lamb waves in the resonant cavity, which is also useful for reducing energy dissipation and device size.

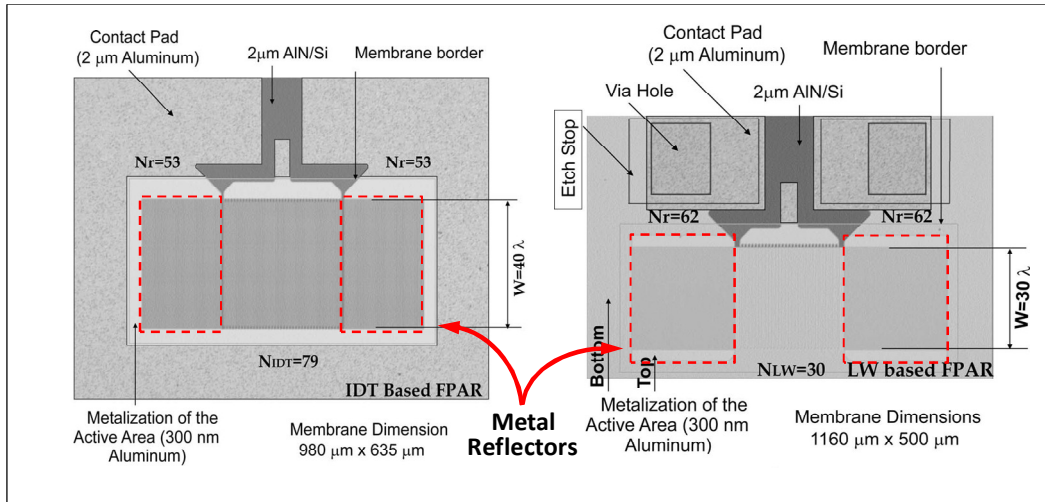


Figure 2.4 Top views of (a) an IDT-based thin film plate acoustic resonator (FPAR) and (b) an LW-LFE-based FPAR [7]. Both devices use quarter-wavelength metal strips as distributed Bragg reflectors placed on each side of the transducer.

### 2.3 Material Properties of Aluminum Nitride

Aluminum nitride (AlN) is an intrinsically-poled, non-ferroelectric material (no Curie point) which has been reported to retain its piezoelectric properties at temperatures above 1000°C [42, 43]. AlN does not occur in nature and was first synthesized by F. Briegleb and A. Geuther in 1862 by heating aluminum in a nitrogen atmosphere at 700°C [44]. This section reports on general properties of thin-film AlN.

AlN can crystallize in both wurtzite and zinc-blende structures. The hexagonal wurtzite crystal structure is shown in Figure 2.5 with covalent bonds and lattice constants  $a = 3.112 \text{ \AA}$  and  $c = 4.982 \text{ \AA}$  [45].

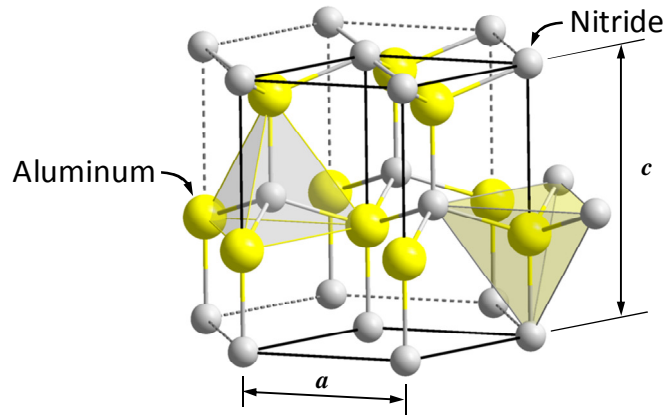


Figure 2.5 Wurtzite hexagonal AlN crystal structure [46]. The yellow spheres represent aluminum atoms and the gray ones represent nitride atoms.

For this (0002)-oriented AlN film, the  $c$ -axis is normal to the substrate surface and the plane parallel to the substrate surface is the closest-packed basal plane, with either all Al or N atoms.

Due to its unique properties, aluminum nitride is a potential material for many applications. Table 2.1 lists some important material properties of the wurtzite AlN. AlN is stable to very high temperature in inert atmospheres and has a relatively high mechanical strength up to 500 MPa even at 1400°C [47]. In air, surface oxidation occurs above 700°C. But this thin layer of aluminum oxide protects the material up to 1370°C at which the bulk oxidation occurs. In hydrogen and carbon dioxide atmospheres, AlN is stable up to 980°C. Together with its exceptional chemical stability, AlN is an excellent candidate for developing MEMS technology for harsh environment applications.

For optoelectronic applications, AlN thin film is a common buffer layer in the growth of gallium nitride (GaN) film on silicon due to its small lattice and thermal mismatches with the silicon substrate. Hexagonal wurtzite structured single-crystalline AlN has a wide direct bandgap of 6.2 eV. When alloyed with GaN, it spans a continuous range of direct band gap energy corresponding to the visible green/blue light spectrum into the ultraviolet (UV) wavelength. This group III-nitride system (GaN, AlN, and InN) is promising for optoelectronic devices, such as light-emitting diodes (LEDs), laser diodes, and photo-detectors [48]. Besides, these wide bandgap III-nitride semiconductors usually have a very high breakdown voltage and electron saturation drift velocity [45, 47]. Together with the negative electron affinity, AlN demonstrates tremendous potential applications for high-power electronic devices.

Like Al<sub>2</sub>O<sub>3</sub> and HfO<sub>2</sub>, AlN has very high dielectric constant and is therefore commonly used as a gate dielectric and insulation layer which is responsible for eliminating parasitics. Besides, AlN is one of the few non-metallic solids with a high thermal conductivity of 320

W/m·K theoretical value [49]. This properties makes AlN a successful packaging material to dissipate heat generated in microelectronic devices.

In recent decades, the hexagonal polycrystalline AlN film exhibiting high quality piezoelectric properties for the transduction of acoustic waves has attracted great attention for RF applications because it can provide a simultaneous solution for high acoustic phase velocity, low motional resistance, and post-CMOS compatibility [50, 51]. Compared with other piezoelectric thin films, AlN has nearly twice the acoustic wave velocity and is therefore better than quartz, LiNbO<sub>3</sub>, PZT, and ZnO with respect to high frequency applications. For RF applications, the temperature coefficient of the piezoelectric layer affects the thermal drift of the resonator. AlN has a lower temperature coefficient compared with ZnO and can be compensated by introducing a specific thickness of silicon dioxide (SiO<sub>2</sub>) layer. A high thermal conductivity mentioned previously also enhances the power handling capability of the device.

A thin-film AlN S<sub>0</sub> mode Lamb wave shows a slightly lower piezoelectric coupling when compared to other piezoelectric films, such as ZnO or LiNbO<sub>3</sub>. This property limits the synthesis of bandpass filters used for current cellular phone front-end architectures which typically require 2 to 5% fractional bandwidth. However, it offers the building blocks to synthesize narrowband filters used in the filter bank architecture discussed in Chapter 1. In these aspects, AlN thin film shows excellent properties and is therefore employed for the demonstration of CMOS-compatible RF resonator/filter technology in this thesis.

Table 2.1 AlN material properties

Property	Symbol	Value	Reference
Density (kg/m <sup>3</sup> )	$\rho$	3260	[39]
Melting point (°C)	$T_m$	> 2200	[52, 53]
Band gap (eV)	$E_g$	6.2	[39]
Breakdown voltage (kV/mm)	$E_B$	~ 140	[54]
Dielectric constant (F/m)	$\epsilon_r$	8.2 – 8.9	[39]
Thermal conductivity (W/ m·K)	$\kappa$	200 – 320	[52, 53]
Resistivity (Ω-cm)	$\rho_e$	10 <sup>13</sup>	[52, 53]
Reflective index	$n$	2.15	[54]
Temperature coefficient (longitudinal) (ppm/°C)	TCF	-25	[55]
Acoustic wave velocity (longitudinal) (m/s)	$v_l$	11000	[39]
Acoustic wave velocity (shear) (m/s)	$v_s$	5800	[39]
BAW coupling coefficient (%)	$k_t^2$	6.5	[55]

# Chapter 3

---

## Fine Frequency Selection Techniques for AIN Lamb Wave Resonators

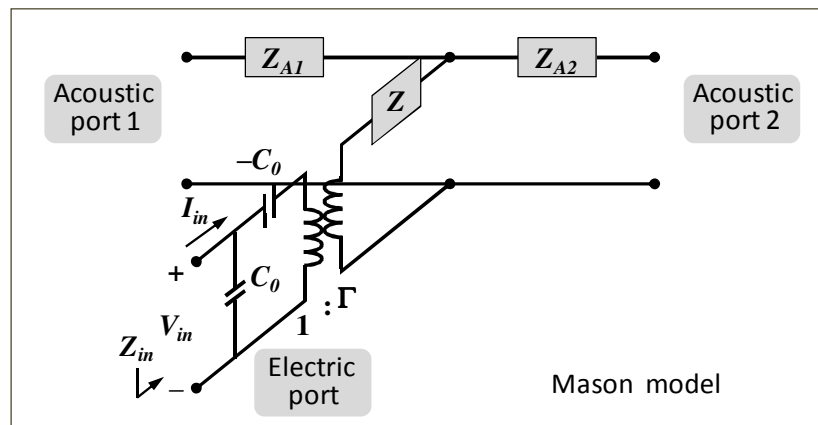
Chapter 3 provides an overview of resonator basics and the equivalent circuit model. The Butterworth-VanDyke (BVD) model is commonly used to represent a one-port resonator. Quality factor  $Q$  and electromechanical coupling  $k_t^2$  are two important properties used to describe device performance and will be discussed. This chapter will also present a baseline silicon micromachining process used to fabricate Lamb wave resonators studied in this thesis. Experimental study of four different fine frequency selection techniques will be discussed, including the overhang adjustment. At the end of this chapter, fine control of the relative center frequency of resonators in an array will be demonstrated.

### 3.1 Resonator Basics

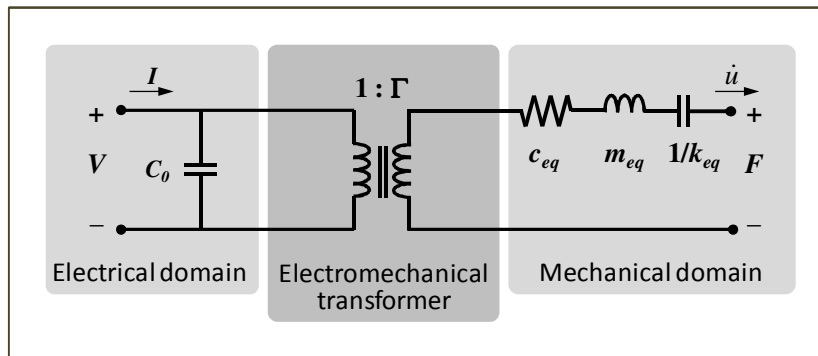
A piezoelectric MEMS resonator is an elastic micro-structure utilizing piezoelectric transduction to excite acoustic vibrations at certain frequencies and transfer energy between electrical and mechanical domains. This micro-structure (resonator) can be made into various shapes, together with different electrode topologies to pick up or suppress specific vibration modes at different frequencies. The electric fields drive the piezoelectric resonator into a specific mode through the converse piezoelectric effect; when it vibrates, the deformations of the resonator induce periodic charges which can be picked up by output electrodes through the direct piezoelectric effect. Establishing the equivalent circuit model of an electromechanical resonator is useful to evaluate device performance and to apply in the circuit analysis. Some material properties can also be calculated from the extracted lumped parameters from the measurement.

### 3.1.1 Mason Model

The Mason model is a well-known electromechanical transfer model used to describe the electrical behavior of an acoustic resonator. It separates the piezoelectric material into two acoustic ports and one electric port, and converts the interaction between electrical and mechanical domains through an ideal electromechanical transformer with a turn ratio  $\Gamma$ . Figure 3.1(a) shows the Mason model of a piezoelectric layer used in the network theory approach. Most of the difficulties in deriving the wave propagation through the acoustic layer can be overcome by applying this network theory approach [56]. This model can be further simplified as in Figure 3.1(b) to represent a single-degree-of-freedom (1-D) electromechanical resonator. The impedance is replaced by the  $R$ - $L$ - $C$  elements corresponding to their equivalent  $c$ - $m$ - $k$  mechanical terms.



(a)



(b)

Figure 3.1 (a) The Mason model of a piezoelectric layer used in the network theory approach. (b) A lumped equivalent parameter model for a 1-D electromechanical resonator.

When an AC signal is applied to the left side of Figure 3.1(b), the electric field induces corresponding mechanical strain (also stress) at the right side which causes the dilation or

contraction of the resonator through the ideal electromechanical transformer. If the signal frequency coincides with one of the natural frequencies of the structure, the specific vibration mode will be excited. The static capacitance  $C_0$  is due to the dielectric property of the material contained between electrodes and is in parallel to the electromechanical resonator represented by its equivalent electrical elements.

### 3.1.2 One-Port Resonator Circuit Model

A one-port 1-D electromechanical resonator using metal electrodes can be presented by the Butterworth Van Dyke (BVD) equivalent model shown in Figure 3.2.

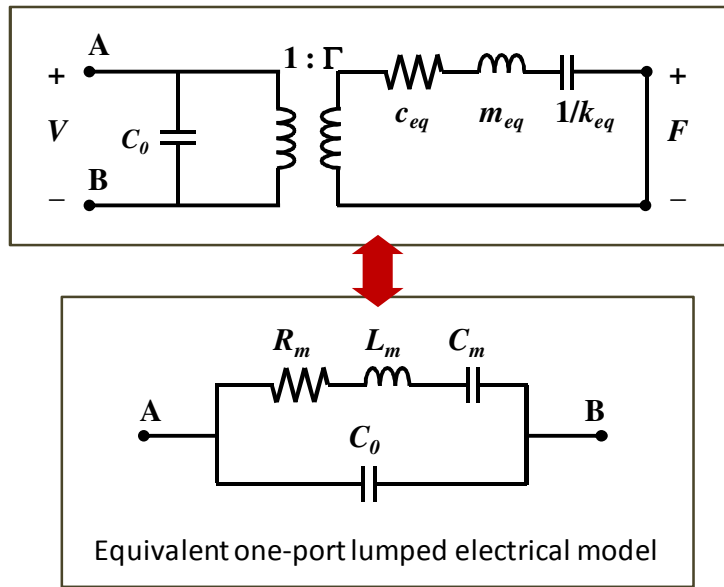


Figure 3.2 Lumped BVD equivalent model for a one-port 1-D electromechanical resonator.

The resonator is represented with a motional resistor  $R_m$ , a motional inductor  $L_m$ , and a motional capacitor  $C_m$  in parallel with a geometric (static) capacitance of the structure  $C_0$  which is irrelevant to the vibration of the resonator. The elements  $R_m$ ,  $L_m$ , and  $C_m$  in the "motional branch" are determined by the acoustic properties of the resonator and account for the motional resistance, the inertia, and the elasticity respectively. Equation 3.1 expresses the motional admittance between nodes A and B as

$$Y_{AB} = Y_{in} = \frac{1}{Z_{in}} = \frac{\frac{C_0}{C_m} + j\omega C_0 R_m - \omega^2 C_0 L_m + 1}{R_m + j\omega L_m + \frac{1}{j\omega C_m}} \quad (3.1)$$

Assuming the ideal case with no resistive element ( $R_m = 0$ ), when the admittance is infinite, the series resonance frequency  $f_s$  (or just "resonance frequency") occurs and can be expressed by  $C_m$  and  $L_m$  as given in Equation 3.2. When the admittance is zero, the parallel resonance frequency  $f_p$  (also called as anti-resonance frequency) occurs and can be expressed by  $L_m$ ,  $C_m$ , and  $C_0$  in Equation 3.3.

$$f_s = \frac{\omega_s}{2\pi} = \frac{1}{2\pi} \frac{1}{\sqrt{L_m C_m}} \quad (3.2)$$

$$f_p = \frac{\omega_p}{2\pi} = \frac{1}{2\pi} \sqrt{\frac{C_0 + C_m}{L_m C_0 C_m}} \quad (3.3)$$

### 3.1.3 Quality Factor ( $Q$ )

A typical resonator response is illustrated in Figure 3.3. The quality factor  $Q$  is a dimensionless parameter that is generally expressed as the ratio of the energy stored and the energy dissipated during one oscillation cycle [38]:

$$Q \equiv \omega \cdot \frac{\text{energy stored}}{\text{power dissipated}} = 2\pi \frac{\text{energy stored}}{\text{energy dissipated per cycle}} \quad (3.4)$$

A higher  $Q$  indicates a lower rate of energy dissipation relative to the oscillation frequency. For a resonator, the quality factor indicates how well the input mechanical energy is confined in the system during the oscillatory motion. Practically, the device  $Q$  can be derived from the resonator impedance,

$$Q_s = \frac{f}{2} \left| \frac{d\phi_z}{df} \right| \quad (3.5)$$

where  $\phi_z$  is the impedance phase [57]. An alternative method is to directly derive  $Q$  from the  $-3\text{dB}$  bandwidth measurement of the admittance response at the series resonance as shown in Figure 3.3. The quality factor can also relate to the resonator's equivalent electrical parameters as expressed in Equation 3.6:

$$Q_s = \frac{\sqrt{L_m / C_m}}{R_m} \quad (3.6)$$

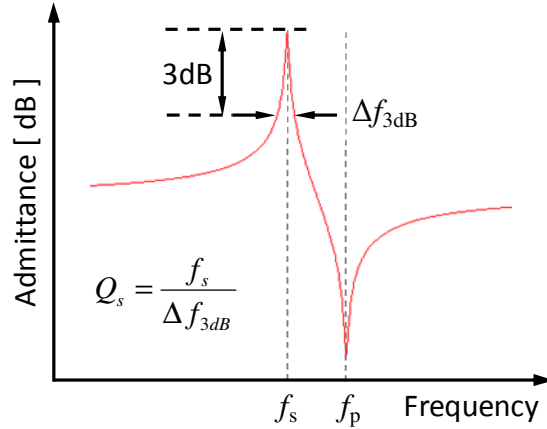


Figure 3.3 A typical admittance response of a resonator. The series resonance frequency is defined as the frequency at maximum conductance, and the parallel resonance is defined as the frequency at the maximum resistance [58].

### 3.1.4 Electromechanical Coupling Coefficient ( $k_t^2$ )

Electromechanical coupling coefficient  $k_t^2$  is another important resonator parameter which is a measure of the energy transduction efficiency between the electrical and mechanical domains. For sufficiently high  $Q$  resonators with small fractional difference between  $f_s$  and  $f_p$  (i.e.,  $f_s \approx f_p$ ), the electromechanical coupling coefficient can be calculated by Equation 3.7 from the impedance spectra obtained from the measurement, or from the equivalent electrical parameters  $C_m$  and  $C_0$ , for the device design perspective [38]:

$$k_t^2 \approx \frac{\pi^2}{4} \frac{f_p - f_s}{f_p} \approx \frac{\pi^2}{8} \frac{C_m}{C_0} \quad (3.7)$$

Since  $k_t^2$  is defined by the fractional difference between resonance and anti-resonance frequencies, this value determines the bandwidth of a ladder-type filter. For filter design, the effective coupling coefficient and the resonator *figure of merit* ( $FOM$ ) have been used to describe the resonator performance as in Equations 3.8 and 3.9 [58]:

$$k_{eff}^2 = \frac{f_p^2 - f_s^2}{f_p^2} \quad (3.8)$$

$$FOM = \frac{k_{eff}^2 \cdot Q}{(1 - k_{eff}^2)} \quad (3.9)$$

Notice that for  $k_t^2 < 6\%$  cases, Equations 3.7 and 3.8 only have a small difference of about 10%.

### 3.2 Lamb Wave Resonator Design

A one-port AlN Lamb wave resonator (LWR) and its equivalent Butterworth-VanDyke (BVD) model are presented in Figure 3.4. The resonator consists of an AlN thin film sandwiched between top and bottom platinum (Pt) electrodes. The top electrode is patterned as IDT fingers to excite Lamb wave propagating in the AlN plate, while the bottom electrode is a single piece rectangular plate. In this eight-electrode case, the whole resonator can be modeled as eight sub-resonators connected in parallel with length  $L$ , width  $w$ , and thickness  $T$ . Notice that the capital letters indicate the whole resonator dimension while the small letters refers to the sub-resonator dimension. The resonance frequency is primarily defined by the IDT pitch  $p$  (equal to  $w$ ), and is effectively decoupled from the AlN plate dimension. In this thesis, all Lamb wave resonators use a single bottom electrode to avoid cracks formed in the AlN plate during deposition, and also the edge type reflectors to reduce device size.

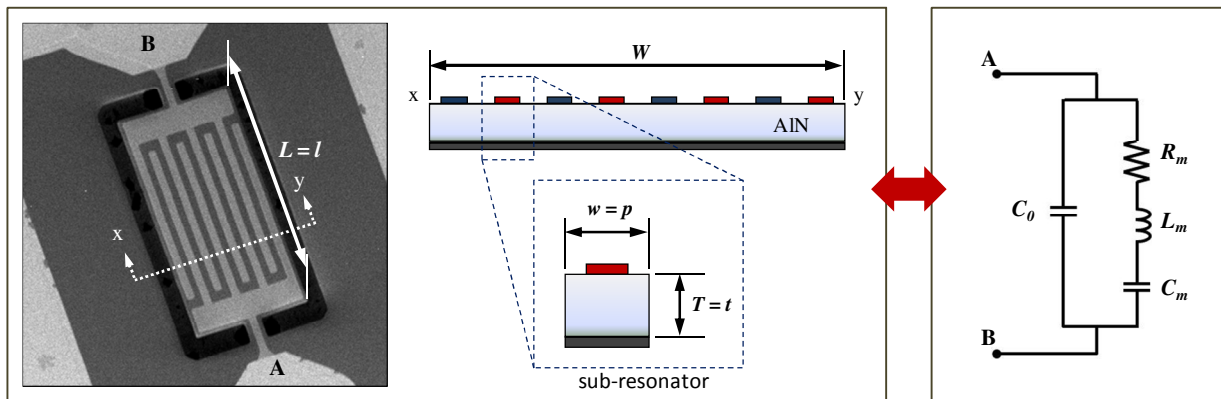


Figure 3.4 A one-port 8-electrode Lamb wave resonator and its equivalent lumped equivalent circuit. The whole resonator can be modeled as eight sub-resonators connected in parallel with length  $L$ , width  $w$ , and thickness  $T$ .

G. Piazza *et al.* have derived the equivalent parameters for contour-mode rectangular plate resonators by the energy method introduced in [26]. By thinking of the LWR as sub-resonators electrically connected in parallel, a one-port LWR can be characterized by the BVD model with device geometry and material properties as

$$\begin{aligned}
R_m &= \frac{1}{n} \frac{\pi T}{8 L} \frac{\rho_{eq}^{1/2}}{E_{eq}^{3/2} d_{31}^2 Q} \\
L_m &= \frac{1}{n} \frac{1}{8} \frac{wT}{L} \frac{\rho_{eq}}{E_{eq}^2 d_{31}^2} \\
C_m &= n \frac{8}{\pi^2} \frac{wL}{T} E_{eq} d_{31}^2 \\
C_0 &\approx n \epsilon_0 \epsilon_{33} \frac{wL}{T} \\
f_s &= \frac{1}{2w} \sqrt{\frac{E_{eq}}{\rho_{eq}}}
\end{aligned} \tag{3.10}$$

where  $L$  ( $=l$ ),  $T$  ( $=t$ ), and  $w$  refer to the length, thickness, and width of the sub-resonator respectively;  $n$  is the number of sub-resonators (IDT numbers);  $\epsilon_0$  is the permittivity in the free space,  $\epsilon_{33}$  is the dielectric constant of AlN along the c-axis;  $E_{eq}$  and  $\rho_{eq}$  are the equivalent elastic modulus and mass density of the Pt/AlN/Pt layers;  $d_{31}$  is the piezoelectric coefficient maps the c-axis electric field to in-plane strain.

The design of a Lamb wave resonator usually starts from the selection of the required center frequency by defining the in-plane geometry and the required IDT pitch, and then adjusting the motional resistance for impedance matching to the applied RF circuit.

### 3.3 Device Fabrication

In the last two decades, semiconductor manufacturing processes used to fabricate integrated circuit have been adapted to fabricate MEMS devices for sensor and actuator applications. The major concepts and principles include: thin film deposition, doping, microlithography, etching, polishing, bonding, and molding. This section describes the five-mask baseline process flow to fabricate AlN Lamb wave resonators by means of silicon micromachining processes.

The five-mask baseline process flow proposed in Figure 3.5 is a modification from previous work used to fabricate contour-mode resonators [26]. Although aluminum (Al), molybdenum (Mo), and tungsten (W) all have been widely used in the fabrication of AlN resonators, this study uses platinum (Pt) as the electrode material since it is inert to all gasses and acids used in the microfabrication process.

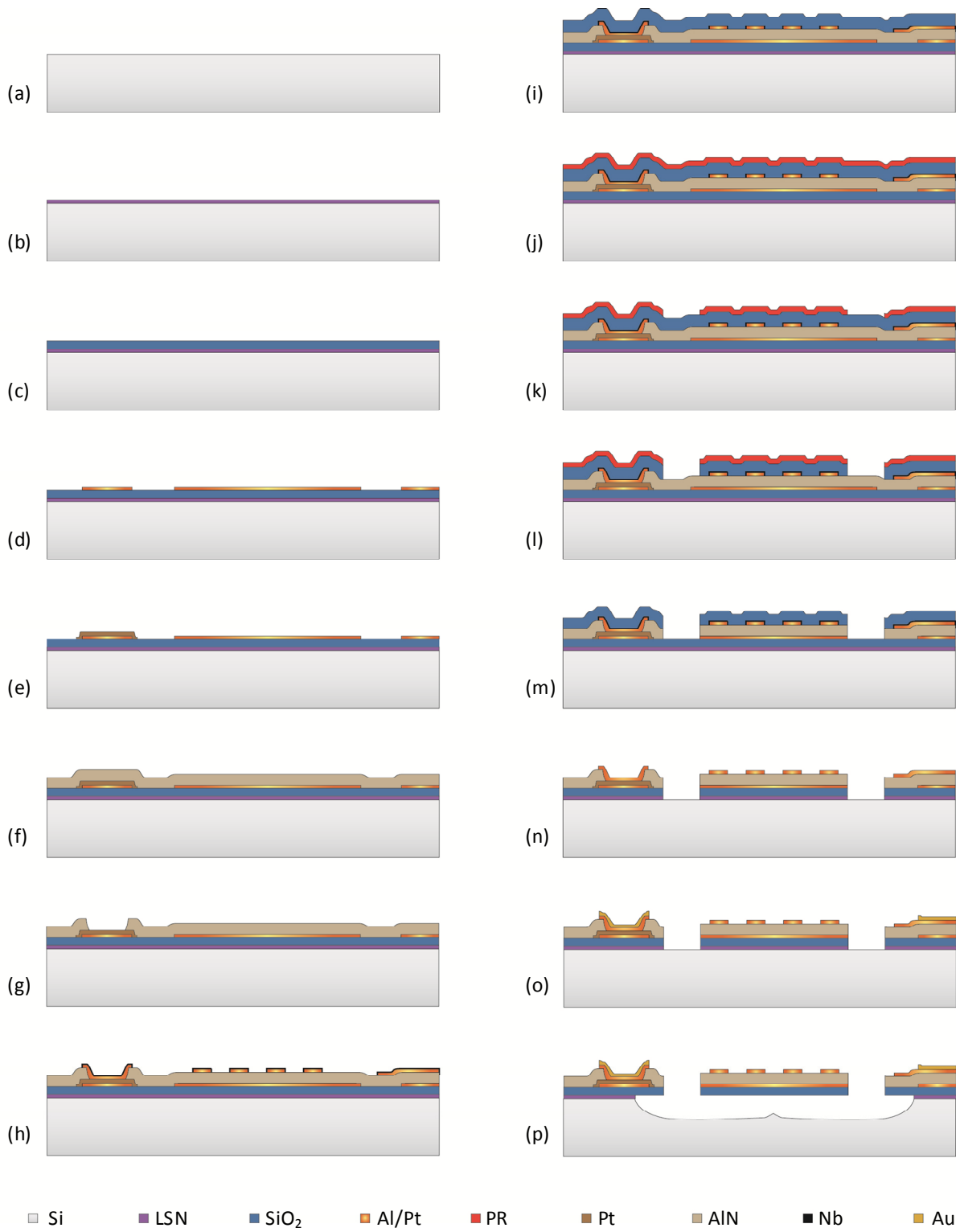


Figure 3.5 The five-mask baseline microfabrication process flow for AlN LWRs.

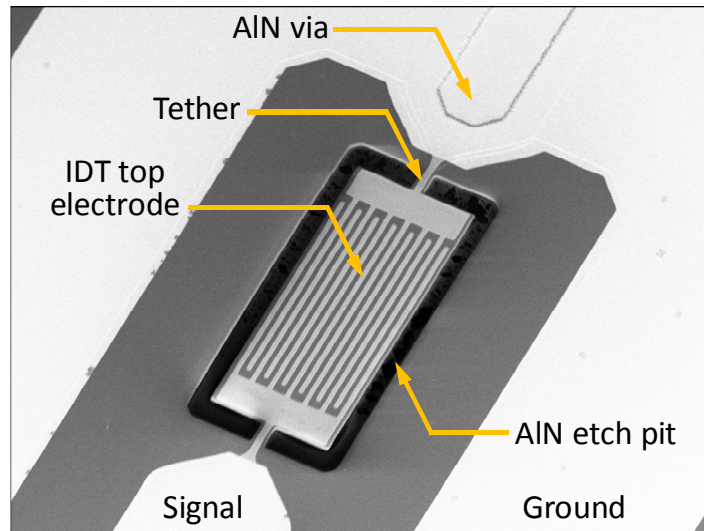
First, a 300 nm low-stress nitride (LSN) layer, used to reduce electrical feed-through and deleterious parasitics, and a 1  $\mu\text{m}$  low temperature oxide (LTO) layer, used for thermal compensation, were deposited on 10000  $\Omega\text{-cm}$  high resistivity six-inch silicon wafers (Figure 3.5(a)~(c)). Then, 1  $\mu\text{m}$  OCG-825 (G-line) photoresist was spin coated on the wafer followed by another 1  $\mu\text{m}$  OiR-10i (I-line) photoresist. This dual layer PR lift-off process results in small undercut and ensures a clean metal edge since G-line is more sensitive to the UV-light. A 0.1  $\mu\text{m}$ -thick Cr/Pt bottom electrode was deposited by evaporation on the patterned dual layer PR. Figure 3.5(d) applies after the ultrasonic bath lift-off process. If using aluminum as the bottom electrode material, an extra etch stop layer (Figure 3.5(e)) is necessary before sputter deposition of the AlN layer since the wet etch selectivity between Al and AlN is relatively low.

The crystal orientation of AlN films and, consequently, the piezoelectric response, depend strongly on surface roughness and texture of the bottom electrode, so an in-situ surface treatment of the bottom Pt electrode in low-power RF discharge, prior to AlN deposition, was performed to reduce the Pt surface roughness. Then, as shown in Figure 3.5(f), the 1,500 nm thick piezoelectric AlN film was deposited using an AC reactive sputtering tool with a dual cathode S-Gun magnetron from Tegal Corporation. Good surface roughness and process control enabled formation of AlN films exhibiting a strong (0002) texture with a rocking curve Full-Width Half-Maximum, or FWHM, of  $1.3^\circ$  and intrinsic stress less than  $\pm 50$  MPa.

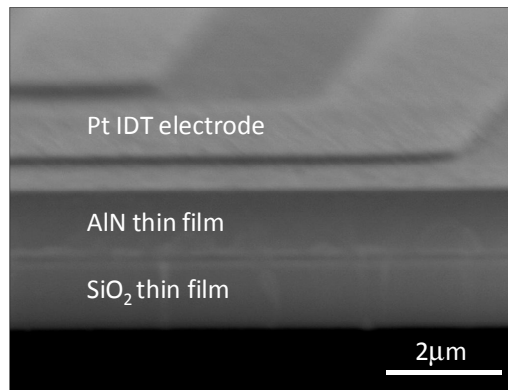
After the AlN deposition, vias were patterned and opened by wet isotropic etch (Figure 3.5(g)). Standard I-line developer OCG-4262 at  $50^\circ\text{C}$  and phosphoric acid at  $160^\circ\text{C}$  are two etchants suitable for AlN wet etching. Then, the dual layer photoresist was applied and patterned for top electrode lift-off process. The top IDT electrode made of Cr/Pt was deposited and patterned on the AlN and also the via to reach the bottom electrodes as illustrated in Figure 3.5(h). If aluminum is the chosen material for top electrode, a thin layer of niobium (Nb) can be deposited right after Al deposition to protect the surface from damage in the silicon dioxide hard mask deposition step.

A PECVD (Plasma Enhanced Chemical Vapor Deposition) silicon dioxide layer was then deposited at  $350^\circ\text{C}$  and patterned in a  $\text{C}_4\text{F}_8$ -based etch system as the hard mask (Figure 3.5(i)~(l)). The sidewall angle of the oxide hard mask can be transferred to the AlN sidewall angle, which is critical for the quality factor of the Lamb waver resonators. Photoresist used to define the hard mask is then removed to prevent re-sputtering of organics on the sidewall. AlN dry etch is performed in a chloride-based Reactive Ion Etching (RIE) to define AlN resonators. Figure 3.5(m) results after these steps. After the AlN etch, the remaining oxide hard mask is removed by a  $\text{CF}_4$ -based dry etch which also simultaneously defines the thermal compensation oxide layer (Figure 3.5(n)). A thick layer of Al or Au was deposited on certain parts of top electrodes as bond/probe pad to improve the conductivity as shown in Figure 3.5(o).

Finally, in Figure 3.5(p), the devices were diced and released from the substrate using a dry isotropic  $\text{XeF}_2$  etching. Figure 3.6 shows the SEM images of a typical Lamb wave resonator and its cross-section. All the above mentioned steps were processed in the Berkeley Marvell Nanofabrication Laboratory.



(a)



(b)

Figure 3.6 SEM images of (a) a typical LWR and (b) its cross-section view with a thin silicon dioxide layer for temperature compensation.

### 3.4 Fine Frequency Selection Study for AlN Lamb Wave Resonators

The resonance frequency of a typical AlN LWR shown in Figure 3.7 is mainly determined by the IDT electrode pitch  $p$ , and the width of the resonant cavity  $W$ . The use of IDT electrodes and  $S_0$  mode Lamb wave in a thin film AlN structure effectively decouple the resonance

frequency of the device from its overall dimension and enable lithography-based frequency selection [51]. In the conventional design, resonator width  $W$  and electrode pitch  $p$  are optimized to create an ideal cavity for the desired wavelength and thus the desired center frequency. However, 0.05 to 0.1% channel spacing for the proposed filter bank architecture (Figure 1.1) requires changes in the IDT dimensions of a few nm per channel, which is impractical.

To achieve fine control of the *relative* frequency of each resonator in an array to 0.05 to 0.1% without post-process trimming poses a tremendous challenge. In this section, four possible fine frequency selection techniques for AlN LWRs were studied, including adjusting electrode number  $n$ , device length  $L$ , electrode coverage  $\eta$ , and the AlN overhang  $OH$ . All of these techniques utilize lithography-based dimensional or design changes without relying on post-process trimming. Conclusions are based on experimental results from measurements of over 200 devices fabricated for this study.

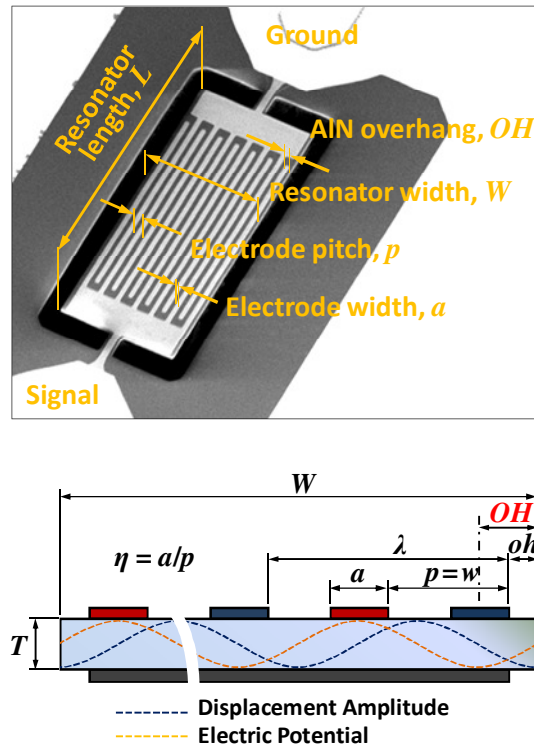


Figure 3.7 Micrograph and cross-section of a typical AlN Lamb wave resonator. The maximum electrode potential coincides with IDT electrode position, while the displacement maximum occurs at the midpoints of two adjacent electrodes and also at the edges of the AlN plate.

### 3.4.1 Adjusting Electrode Number, $n$

For the first study, three groups of resonators with different frequencies were designed and fabricated, all with AlN thickness of  $1.5\ \mu\text{m}$  and fixed dimensions except the electrode number  $n$ . If mass loading is neglected, there should be no effect on the resonance frequency while  $n$  increases. However, when it is considered, the resonance frequency shows a strong dependence on  $n$  as shown in Figure 3.8. For 800 MHz resonators, when  $n$  increases from 3 to 18, the normalized device mass (normalized to 3-electrode devices)  $\Delta M$  increases by 500%, and the normalized frequency  $\Delta f$  decreases by 4%. Increasing electrode number  $n$  causes more spurious modes to appear within a small range of frequency. Resonator parameters, including  $C_0$  and  $R_m$ , both vary, which makes this technique difficult to use in filter design.

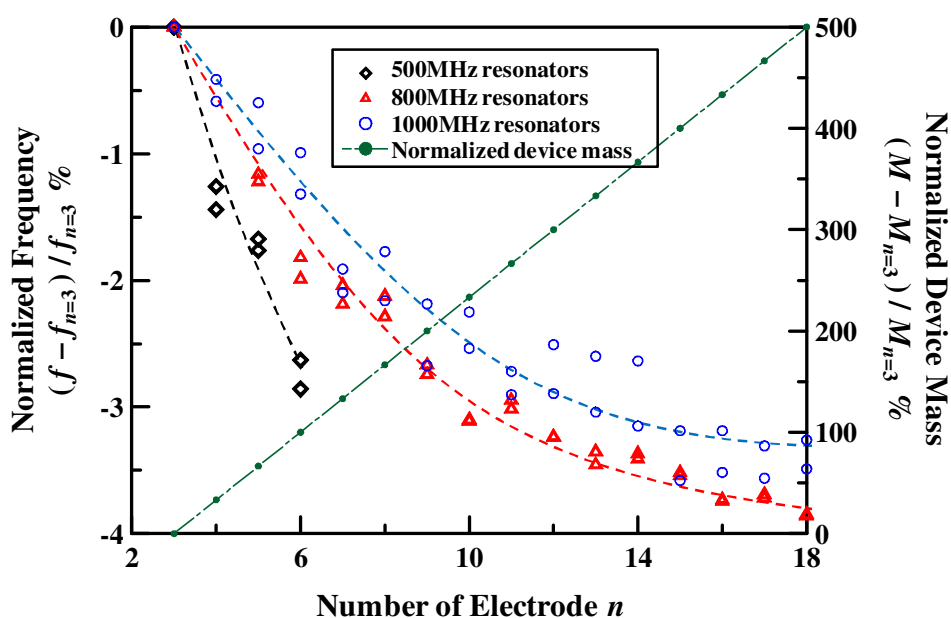


Figure 3.8 Frequency shift versus electrode number,  $n$ . The dashed lines are a polynomial fit to the data.

### 3.4.2 Adjusting Device Length, $L$

For the second study, data from three groups of resonators designed at 500, 800, and 1000 MHz were collected. In each group, resonator dimensions are all fixed except the length  $L$ , which varies from  $3\lambda$  to  $18\lambda$ . According to the theoretical analysis, the resonance frequency of LWR is not a function of  $L$ . Although not very clear, the trend presented in Figure 3.9 shows that the normalized device mass (normalized to  $L = 3\lambda$  devices)  $\Delta M$  increases by 240%, and the normalized frequency  $\Delta f$  decreases by only 0.6% when  $L$  increases from  $3\lambda$  to  $18\lambda$ . These results indicate that this technique is inefficient and very difficult to use to predict the frequency shift. From Equation 3.10, it is clear that  $C_0$  and  $R_m$  are proportional and inversely proportional to  $L$

respectively. It is also important to point out that the resonator performance ( $Q$  and  $k_t^2$ ) degraded significantly when  $L > 10\lambda$ .

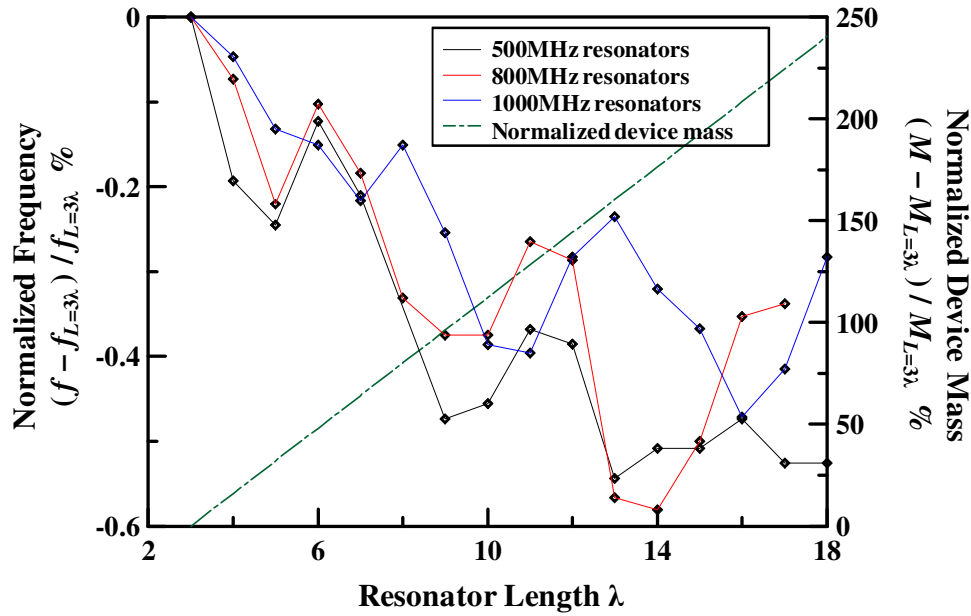


Figure 3.9 Frequency shift versus device length,  $L$ .

### 3.4.3 Adjusting Electrode Coverage, $\eta$

The electrode coverage,  $\eta$ , is defined by  $\eta = a/p = 2a/\lambda$ , where  $a$  is the electrode width. Experimental data of 500, 800, and 1000 MHz resonators with Pt electrode coverage ranging from 0.1 to 1.0 are shown in Figure 3.10. When  $\eta$  increases from 0.3 to 1.0, the normalized device mass (normalized to  $\eta = 0.5 = \lambda/4$ )  $\Delta M$  increases by 35% (for the 500 MHz case), and the normalized frequency  $\Delta f$  decreases by 12%. This frequency shift is mainly due to the mass loading of the electrodes, and is thus very sensitive to the electrode material and thickness chosen.

Although  $\eta$  is usually not considered as a parameter that affects the center frequency during the resonator design, it plays an important role for calculating the electromechanical coupling  $k_t^2$ . Figure 3.11 plots the predicted and measured normalized  $k_t^2$  and  $R_m$  versus electrode coverage  $\eta$ . Although large  $\eta$  results in smaller  $R_m$ , the maximum  $k_t^2$  occurs when the electrode coverage  $\eta = 0.74$  [51]. Note that device performance degrades significantly when  $\eta$  is less than 0.3. For design consistency, electrode coverage elsewhere in this thesis is designed to be 0.5. This technique affects many other resonator parameters in terms of  $Q$ ,  $C_0$ ,  $R_m$ , and  $k_t^2$  and therefore is not a good option for fine frequency control.

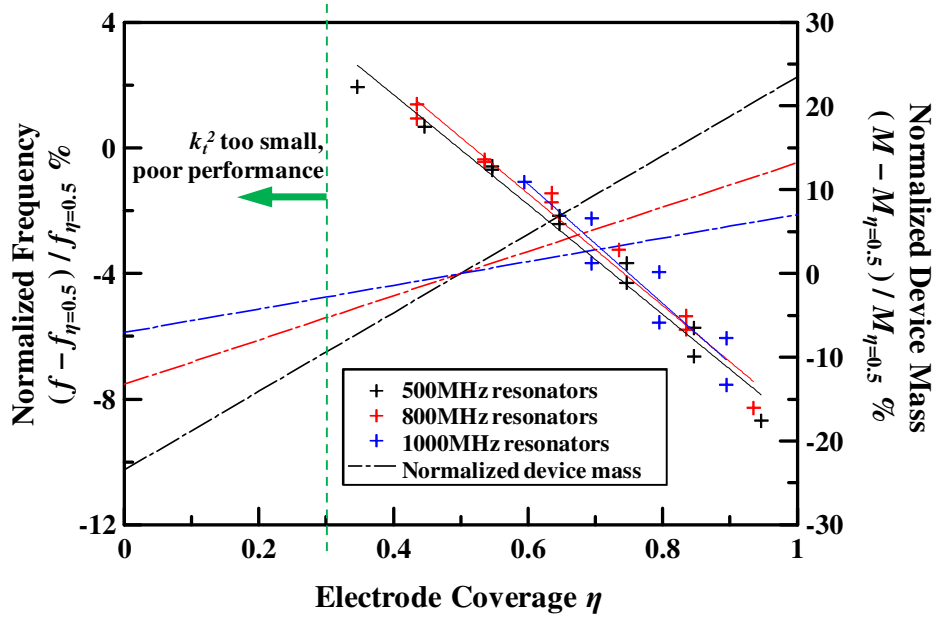


Figure 3.10 Frequency shift versus electrode coverage,  $\eta$ . The solid lines are linear fits to the data.

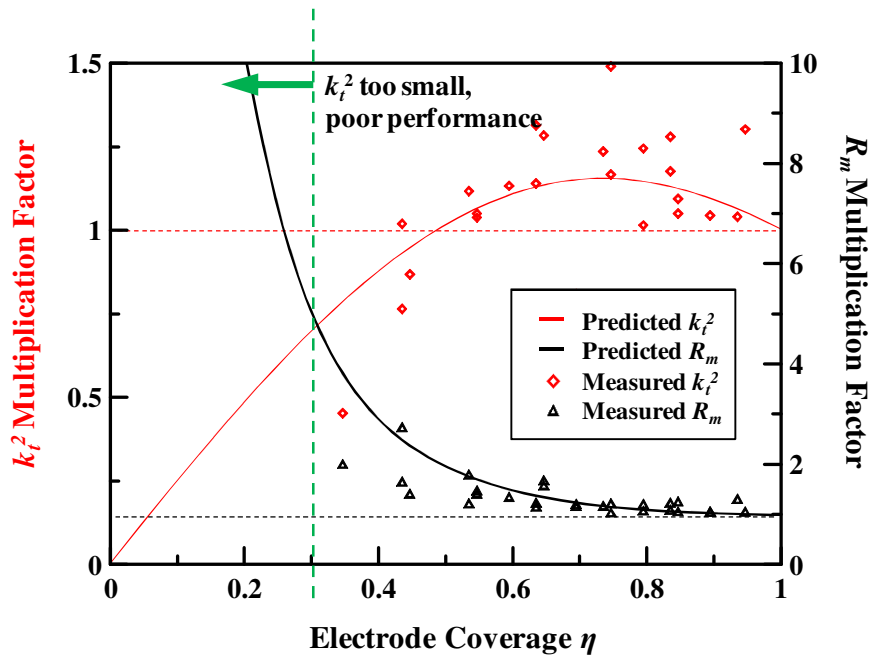


Figure 3.11 Normalized  $R_m$  and  $k_t^2$  versus electrode coverage  $\eta$ .  $R_m$  and  $k_t^2$  are both normalized to the cases when  $\eta=1$ . Device performance degrades significantly when  $\eta$  is smaller than 0.3.

All of these frequency selection techniques affect the center frequency and other key resonator parameters ( $Q$ ,  $C_0$ ,  $R_m$ , and  $k_t^2$ ) to various degrees and are therefore difficult to employ in the channel-select filter bank application. A technique that only shifts the resonance frequency but not other device parameters is desired.

#### 3.4.4 Adjusting AlN Overhang, $OH$

In a given piezoelectric plate, many different acoustic modes can be excited. The position and pitch of the electrodes determine which mode(s) are excited and which are suppressed. For Lamb wave mode resonators in which the acoustic waves propagate perpendicular to the direction of the device width, the pitch of IDT electrodes,  $p$ , determines the frequency to be excited,

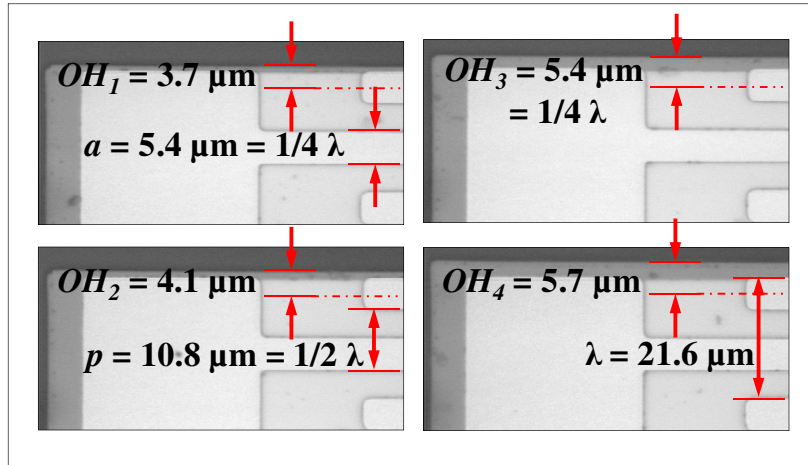
$$f = \frac{v_a}{\lambda} = \frac{v_a}{2p} \quad (3.8)$$

where  $v_a$  is the Lamb wave phase velocity, and  $\lambda$  is the wavelength. For LWRs using edge-type reflectors, the ideal resonant conditions are met when the center of the IDT electrode coincides with the maximum of the electrode potential and the minimum of the displacement amplitude (Figure 3.7) [59]. Additionally, the displacement maxima must be located at the edges of the AlN plate. When these ideal resonant conditions are met, the desired mode is excited most strongly.

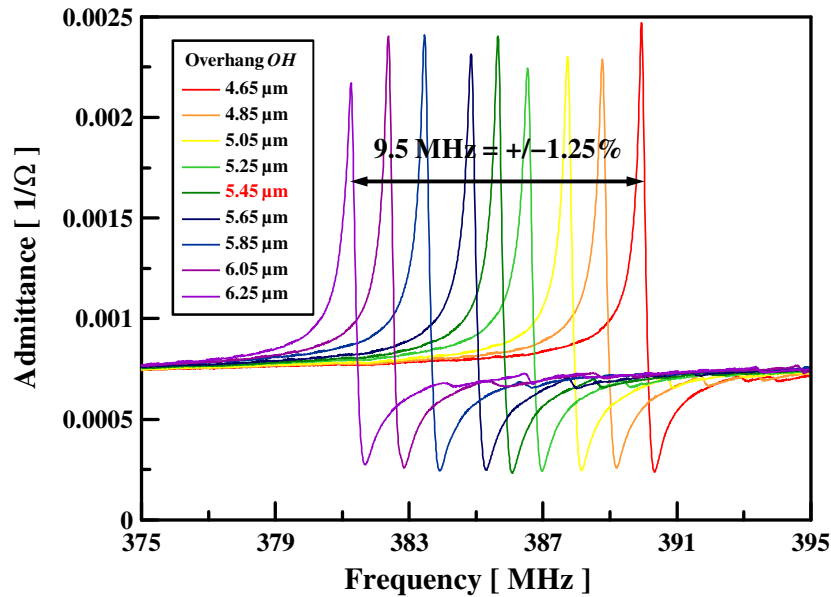
Therefore, to efficiently excite a specific mode, the *ideal* overhang  $OH$ , the dimension measured from the center of the outermost electrode to the edge of the plate, must be set to one-quarter wavelength ( $0.25\lambda$ ) so that the electrode potential and the displacement maximum match the IDT electrode pitch. When the overhang dimension is increased or decreased independently of the IDT pitch, other modes *very* close to that ideal condition can also be excited even though IDT electrodes are not placed at the ideal position. By adjusting overhang independently of the IDT pitch, the center frequency is then determined by the total width of the plate,  $W$ , and the number of IDT electrodes,  $n$ :

$$f = \frac{v_a}{\lambda} = \frac{n \cdot v_a}{2W} \quad (3.9)$$

Figure 3.12 shows measured admittances of a nine-resonator array designed at 385 MHz. Each resonator has eight electrodes ( $n=8$ ) with the same electrode pitch ( $p=\lambda/2=10.8\ \mu\text{m}$ ), but the overhang varies from 4.65 to 6.25  $\mu\text{m}$  in 0.2  $\mu\text{m}$  increments. All peaks are clean with  $k_t^2 \sim 0.3\%$  and quality factors between 1500 and 1800. Thus, a 9.5 MHz frequency shift due to the change of overhang dimension without affecting device performance is verified. The maximum allowed frequency shift by adjusting overhang dimension depends on the distance in frequency to the next spurious mode.



(a)



(b)

Figure 3.12 (a) Four resonators with the same electrode pitch but slightly different overhang dimensions. (b)  $S_{11}$  admittance response of a nine-resonator array ( $n = 8$ ). All resonators have the same electrode pitch but with  $0.2 \mu\text{m}$   $OH$  increments.

Because the overhang adjustment technique evenly distributes the effects of the  $2\Delta OH$  dimension changes (one on each side) across all pairs of IDT electrodes, the sensitivity of the resonance frequency to the value of  $2\Delta OH$  is reduced and practical fine frequency selection becomes possible with standard semiconductor lithography. Measurements of two groups ( $n = 4$  and  $n = 8$ ) of devices designed at 385 MHz, with AlN thickness of  $1.5 \mu\text{m}$ , Lamb mode wavelength  $\lambda = 21.6 \mu\text{m}$ , and overhang  $OH$  varying from  $0.2\lambda$  to  $0.3\lambda$ , are presented in Figure

3.13. When  $OH$  increases from  $0.2\lambda$  to  $0.3\lambda$ , the normalized frequency (normalized to devices with  $OH = 0.25\lambda$ )  $\Delta f$  decreases by 2.5% and 6% for  $n = 8$  and  $n = 4$  cases respectively. This indicates that the effectiveness of the change in overhang also depends on the number of IDT electrodes and the corresponding width of the cavity. Devices with larger  $n$  are less sensitive to the same amount of changes in overhang. In other words, the resonance frequency of LWRs with larger  $n$  can be more precisely adjusted by the same overhang increment than those with smaller  $n$ .

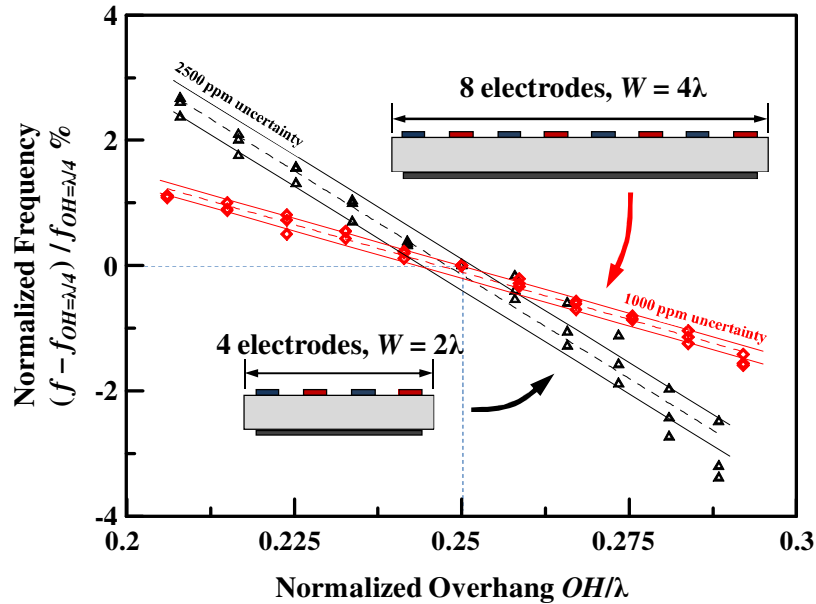


Figure 3.13 Frequency shift versus AlN overhang. Devices with larger  $n$  are less sensitive to the same amount of  $\Delta OH$ , i.e., more precise frequency control.

Based on these experimental data, the change in center frequency shows a clear dependence on the dimension of the cavity ( $W$ ), while the electrode pitch and design determine the efficiency with which the modes are excited. The excitation of the spurious mode is not as efficient as that of the main mode since the electrode position is not ideal for exciting these modes. While this technique effectively "detunes" the acoustic cavity by adjusting  $OH$  around  $\lambda/4$ , experimental results suggest the center frequency can be adjusted linearly by up to 5% with no significant effect on other device parameters including  $Q$ ,  $R_m$ ,  $C_0$ , and  $k_t^2$ . This range depends on the distance in frequency to the next spurious mode. Usually, devices with more electrodes have more spurious modes and denser spacing [59]. The linearity and predictability, evident in the experimental data in Figures 3.12 and 3.13, make this AlN overhang fine-frequency control technique ideally suited for narrowband filter bank design.



# Chapter 4

---

## Conclusion and Future Work

The piezoelectric AlN Lamb wave resonator technology offers a promising solution to realize a multi-frequency, low motional resistance, and post-CMOS compatible RF front-end architecture. This architecture utilizes closely spaced narrowband filters (filter bank) to fulfill the frequency selection function and brings out another challenge: fine relative frequency control of each channel. Chapter 3 has demonstrated closely and evenly spaced AlN Lamb wave resonators by adjusting the device overhang dimension without post-process trimming. This Chapter will conclude this study and point out some future research directions.

### 4.1 Conclusion

In this thesis, the fine frequency selection based on overhang adjustment has been verified to achieve fine control of the relative center frequency of each resonator in an array to 0.1%. This overhang adjustment technique linearly shifts the center frequency of resonators with the same electrode pitch up to 5% and shows no significant effects on other resonator parameters such as  $Q$ ,  $R_m$ ,  $C_0$ , and  $k_r^2$ . Since the resonant cavity width of a LWR is adjusted independently of the IDT electrode pitch, the effect of the overhang dimension change is decreased by ten times or more, allowing a practical fine-frequency definition with modern semiconductor lithography resolution.

The AlN Lamb wave characteristics are also studied and compared with other acoustic waves. The higher phase velocity of the  $S_0$  mode Lamb wave indicates the possibility of fabricating higher frequency devices with the same IDT pitch. The flat dispersion of the phase velocity shows that the resonance frequency of a LWR is insensitive to AlN thickness and helps to improve the fabrication tolerances towards AlN thickness variation.

A five-mask base-line fabrication process was introduced to fabricate these resonators. The  $f \times Q$  products of typical LWRs have been improved above  $2 \times 10^{12}$ , the same order as that of other commercialized piezoelectric resonator technologies [60], and can be used to fabricate low-cost frequency control devices using standard photolithography resolution up to the lower gigahertz frequency range. These results enable the design and fabrication of highly integrated channel-select filter banks for next-generation radio architectures.

## 4.2 Future Research Directions

There are still many technical challenges worth investigating to realize and improve a narrowband RF filter bank utilizing AlN Lamb wave resonator technology. This final section points out potential research directions for further study.

### 4.2.1 Characterizing Thermal Stability

Chapter 2 mentioned that AlN can maintain a good piezoelectricity above  $1000^\circ\text{C}$  and has a relatively high mechanical strength even at  $1400^\circ\text{C}$ . Together with its exceptional chemical stability, AlN is one of the excellent candidates to realize a wireless sensing platform operating in harsh environments. High-temperature testing to verify the performance and characteristics of AlN LWR would be necessary for harsh environment applications. Besides, the resonance frequencies of piezoelectric AlN resonators are temperature dependent and typically have a temperature coefficient of frequency (TCF) value of  $-25 \text{ ppm}/^\circ\text{C}$ . Temperature compensation is therefore necessary to obtain a satisfactory degree of temperature stability.

### 4.2.2 Investigating Energy Loss Mechanisms

Although enough for synthesizing bandpass filters, the quality factor of piezoelectric AlN MEMS resonators is still one to two orders of magnitude less than that of electrostatic resonators. In order to synthesize channel-select filter bank with 0.1% bandwidth, it is necessary to increase the  $Q$  of individual resonators. The material itself has the potential to realize high- $Q$  devices, but this has not yet been demonstrated experimentally. A better understanding of the energy dissipation mechanisms is therefore necessary in order to account for the difference. Energy dissipation from anchoring tethers, excitation of spurious modes, and viscous damping between AlN and transduction electrodes are three topics worthy of further investigations. Using composite structures along with poly-Si, SiC, or poly-diamond for  $Q$ -boosting is another ongoing research topic related to this thesis.

### 4.2.3 Filter Synthesis with Different Couplings

The electromechanical coupling determines the bandwidth of a filter. AlN LWRs typically exhibiting electromechanical coupling less than 1% are only suitable for synthesizing electrically coupled narrowband filters with 0.5 to 2% bandwidth. On the other hand, band-select RF front-end architectures used in today's wireless communication standards adapt filters with 2 to 5% fractional bandwidth and require stronger coupling in each building block resonator. Improving the AlN thin film quality and orientation can directly affect the electromechanical coupling. As for the filter applications, large fractional bandwidth can be accomplished by using different coupling methods such as mechanical or acoustic couplings, or by introducing passive elements such as inductors for tuning purposes. Different filter topologies including lattice filter and balanced ladder filter are also worth exploring.

### 4.2.4 Integration with IC

To ensure smallest layout area, vertical integration of MEMS devices with electronic circuits is desired. This strategy requires introducing a passivation layer on top of the IC, and another sacrificial layer to release the resonator. A chemical-mechanical polishing (CMP) process will be necessary to smooth the passivation and sacrificial layers for the deposition of the AlN thin film with good crystallinity. Unlike isotropic bulk silicon substrate release used in this study, the use of a sacrificial layer creates a well-defined release area and thus designed tether dimensions which would reduce anchor energy loss and improve device performance.



## Bibliography

- [1] C. T. C. Nguyen, "Frequency-selective MEMS for miniaturized low-power communication devices," *Microwave Theory and Techniques, IEEE Transactions on*, vol. 47, pp. 1486-1503, 1999.
- [2] S.-S. Li, Y.-W. Lin, Z. Ren, and C. T. C. Nguyen, "Self-switching vibrating micromechanical filter bank," *2005 IEEE International Frequency Control Symposium and Exhibition*, pp. 135-141, 2005.
- [3] A. A. Abidi, "Direct-conversion radio transceivers for digital communications," *Solid-State Circuits, IEEE Journal of*, vol. 30, pp. 1399-1410, 1995.
- [4] P. Zhang, L. Der, D. Guo, I. Sever, T. Bourdi, C. Lam, A. Zolfaghari, J. Chen, D. Gambetta, C. Baohong, S. Gower, S. Hart, L. Huynh, T. Nguyen, and B. Razavi, "A CMOS direct-conversion transceiver for IEEE 802.11a/b/g WLANs," in *Custom Integrated Circuits Conference, 2004. Proceedings of the IEEE 2004*, 2004, pp. 409-412.
- [5] C. T. C. Nguyen, "Vibrating RF MEMS for next generation wireless applications," *Proceedings of the IEEE 2004 Custom Integrated Circuits Conference (IEEE Cat. No.04CH37571)*, 01 2004.
- [6] H. Chandrahali, D. Weinstein, L. F. Cheow, and S. A. Bhawe, "High-kappa dielectrically transduced MEMS thickness shear mode resonators and tunable channel-select RF filters," *Sensors and Actuators A (Physical)*, vol. 136, 2007.
- [7] V. Yantchev and I. Katardjiev, "Micromachined thin film plate acoustic resonators utilizing the lowest order symmetric lamb wave mode," *IEEE Transactions on Ultrasonics Ferroelectrics and Frequency Control*, vol. 54, pp. 87-95, Jan 2007.
- [8] G. Piazza, P. J. Stephanou, and A. P. Pisano, "Single-chip multiple-frequency ALN MEMS filters based on contour-mode piezoelectric resonators," *Journal of Microelectromechanical Systems*, vol. 16, pp. 319-328, Apr 2007.
- [9] G. Breed, "There's nothing magic about 50 ohms," *High Frequency Electronics*, Summit Technical Media LLC. 2007.
- [10] <http://www.microwaves101.com/encyclopedia/why50ohms.cfm>.
- [11] R. T. Howe and T. J. King, "Low-temperature LPCVD MEMS technologies," *BioMEMS and Bionanotechnology. Symposium (Materials Research Society Proceedings Vol.729)*, 01 2002.
- [12] L. Rayleigh, "On waves propagated along the plane surface of an elastic solid," *Proc. London Math. Soc.*, s1-17(1): 4-11 1885.
- [13] R. M. White and F. W. Voltmer, "Direct piezoelectric coupling to surface elastic waves," *Applied Physics Letters*, vol. 7, pp. 314-316, 1965.
- [14] Y. Komatsu and Y. Yanagisawa, "A surface acoustic wave filter for color TV receiver VIF," *Electron Devices, IEEE Transactions on*, vol. 24, pp. 230-233, 1977.
- [15] S. Inoue, J. Tsutsumi, T. Matsuda, M. Ueda, O. Ikata, and Y. Satoh, "Analysis and suppression of side radiation in leaky SAW resonators," *IEEE Transactions on Ultrasonics Ferroelectrics and Frequency Control*, vol. 54, pp. 1692-1699, Aug 2007.
- [16] D. Cernadas, C. Trillo, A. F. Doval, J. C. Lopez, B. V. Dorrio, J. L. Fernandez, and M. Perez-Amor, "Non-destructive testing with surface acoustic waves using double-pulse TV holography," *Measurement Science & Technology*, vol. 13, pp. 438-444, Apr 2002.

- [17] G. F. Iriarte, F. Engelmark, I. V. Katardjiev, V. Plessky, and V. Yantchev, "SAW COM-parameter extraction in AlN/diamond layered structures," *IEEE Transactions on Ultrasonics Ferroelectrics and Frequency Control*, vol. 50, pp. 1542-1547, Nov 2003.
- [18] H. Nakahata, A. Hachigo, K. Higaki, S. Fujii, S. I. Shikata, and N. Fujimori, "Theoretical-study on SAW characteristics of layered structures including a diamond layer," *IEEE Transactions on Ultrasonics Ferroelectrics and Frequency Control*, vol. 42, pp. 362-375, May 1995.
- [19] R. Lanz and P. Muralt, "Bandpass filters for 8 GHz using solidly mounted bulk acoustic wave resonators," *IEEE Transactions on Ultrasonics Ferroelectrics and Frequency Control*, vol. 52, pp. 936-946, Jun 2005.
- [20] P. D. Bradley, R. Ruby, A. Barfknecht, F. Geefay, C. Han, G. Gan, Y. Oshmyansky, and J. D. Larson, III, "A 5 mm x 5 mm x 1.37 mm hermetic FBAR duplexer for PCS handsets with wafer-scale packaging," in *2002 IEEE Ultrasonics Symposium. Proceedings (Cat. No.02CH37388)*, 2002.
- [21] R. Ruby, P. Bradley, J. Larson, III, Y. Oshmyansky, and D. Figueredo, "Ultra-miniature high-Q filters and duplexers using FBAR technology," *2001 IEEE International Solid-State Circuits Conference. Digest of Technical Papers. ISSCC (Cat. No.01CH37177)*, 01 2001.
- [22] W. E. Newell, "Face-mounted piezoelectric resonators," *Proceedings of the Institute of Electrical and Electronics Engineers*, vol. 53, pp. 575-81, 1965.
- [23] G. Piazza and A. P. Pisano, "Dry-released post-CMOS compatible contour-mode aluminum nitride micromechanical resonators for VHF applications," in *Hilton Head Workshop '04*, 2004, pp. 37-40.
- [24] P. J. Stephanou, G. Piazza, C. D. White, M. B. J. Wijesundara, and A. P. Pisano, "Piezoelectric aluminum nitride MEMS annular dual contour mode filter," *Sensors and Actuators A-Physical*, vol. 134, pp. 152-160, Feb 28 2007.
- [25] G. Piazza, P. J. Stephanou, M. B. J. Wijesundara, and A. P. Pisano, "Single-chip multiple-frequency filters based on contour-mode aluminum nitride piezoelectric micromechanical resonators," in *TRANSDUCERS '05*, 2005, pp. 2065-2068.
- [26] G. Piazza, P. J. Stephanou, and A. P. Pisano, "Piezoelectric aluminum nitride vibrating contour-mode MEMS resonators," *Journal of Microelectromechanical Systems*, vol. 15, pp. 1406-1418, Dec. 2006.
- [27] D. Weinstein and S. A. Bhave, "Internal dielectric transduction in bulk-mode resonators," *Journal of Microelectromechanical Systems*, vol. 18, pp. 1401-1408, Dec 2009.
- [28] M. Ziaei-Moayyed, D. Elata, E. P. Quevy, and R. T. Howe, "Differential internal dielectric transduction of a Lamé-mode resonator," *Journal of Micromechanics and Microengineering*, vol. 20, Nov 2010.
- [29] M. Ziaei-Moayyed and R. T. Howe, "Higher-order dielectrically transduced bulk-mode ring resonator with low motional resistance," in *IEEE International Frequency Control Symposium (FCS)*, 2010.
- [30] W.-T. Hsu, "Vibrating RF MEMS for Timing and Frequency References," in *Microwave Symposium Digest, 2006. IEEE MTT-S International*, 2006, pp. 672-675.
- [31] M. Lutz, A. Partridge, P. Gupta, N. Buchan, E. Klaassen, J. McDonald, and K. Petersen, "MEMS oscillators for high volume commercial applications," in *Solid-State Sensors, Actuators and Microsystems Conference, 2007. TRANSDUCERS 2007. International*, 2007, pp. 49-52.

- [32] F. D. Bannon III, J. R. Clark, and C. T.-C. Nguyen, "High frequency micromechanical filters," *IEEE Journal of Solid-State Circuits*, vol. 35, pp. 512-526, Apl. 2000 2000.
- [33] M. A. Abdelmoneum, M. U. Demirci, and C. T. C. Nguyen, "Stemless wine-glass-mode disk micromechanical resonators," *Proceedings IEEE 6th Annual International Conference on Micro Electro Mechanical Systems (Cat. No.03CH37426)*, pp. 698-701, 01 2003.
- [34] E. P. Quevy, S. A. Bhave, H. Takeuchi, T.-J. King, and R. T. Howe, "Poly-SiGe high frequency resonators based on lithographic definition of nano-gap lateral transducers," in *Hilton Head Workshop '04*, 2004, pp. 360-363.
- [35] H. M. Liaw and F. S. Hickernell, "SAW characteristics of sputtered aluminum nitride on silicon and gallium arsenide," *1994 IEEE Ultrasonics Symposium. Proceedings (Cat. No.94CH3468-6)*, 01 1994.
- [36] O. Tigli and M. E. Zaghoul, "A novel SAW device in CMOS: design, modeling, and fabrication," *IEEE Sensors Journal*, vol. 7, pp. 219-227, Jan-Feb 2007.
- [37] V. Kochervinskii, "Piezoelectricity in crystallizing ferroelectric polymers: Poly (vinylidene fluoride) and its copolymers (A review)," *Crystallography Reports*, vol. 48, pp. 649-675, 2003.
- [38] J. F. Rosenbaum, *Bulk Acoustic Wave Theory and Devices*, Artech House, Inc., 1988.
- [39] K. Tsubouchi, K. Sugai, and N. Mikoshiba, "AlN material constants evaluation and SAW properties on AlN/Al<sub>2</sub>O<sub>3</sub> and AlN/Si " *IEEE Ultrasonics Symposium Proceedings*, pp. 375-380, 1981.
- [40] I. A. Viktorov, *Rayleigh and Lamb Waves: Physical Theory and Applications*, New York, Plenum Press, 1967.
- [41] Y. Jin and S. G. Joshi, "Excitation of higher-order ultrasonic Lamb wave modes in piezoelectric plates," *Journal of the Acoustical Society of America*, vol. 92, pp. 914-919, Aug. 1992.
- [42] R. C. Turner, P. A. Fuierer, R. E. Newnham, and T. R. Shrout, "Materials for high-temperature acoustic and vibration sensors - a review," *Applied Acoustics*, vol. 41, pp. 299-324, 1994.
- [43] R. Farrell, V. R. Pagan, A. Kabulski, S. Kuchibhatla, J. Harman, K. R. Kasarla, L. E. Rodak, J. P. Hensel, P. Famouri, and D. Korakakis, "High temperature annealing studies on the piezoelectric properties of thin aluminum nitride films," *Microelectromechanical Systems - Materials and Devices Symposium*, 2007.
- [44] J. A. Vanvecht, "Quantum dielectric theory of electronegativity in covalent systems .3. pressure-temperature phase-diagrams, heats of mixing, and distribution coefficients," *Physical Review B*, vol. 7, pp. 1479-1507, 1973.
- [45] G. Yu, *Properties of Advanced Semiconductor Materials: GaN, AlN, InN, BN, SiC, SiGe*, John Wiley & Sons, Inc., New York, 2001.
- [46] [http://en.wikipedia.org/wiki/Aluminium\\_nitride](http://en.wikipedia.org/wiki/Aluminium_nitride).
- [47] L. I. Berger, *Semiconductor Materials*, CRC Press, 1997.
- [48] S. L. Chuang, *Physics of Optoelectronic Devices*, Wiley-Interscience, 1995.
- [49] B.-Y. Liaw, "Diamond and aluminum nitride thin films: synthesis, properties, and some device application," Ph.D. dissertation, Department of Electrical Engineering, University of Missouri-Columbia, USA, 1995.
- [50] R. Ruby, "Review and comparison of bulk acoustic wave FBAR, SMR technology," in *IEEE Ultrasonics Symposium*, 2007, pp. 1029-40.

- [51] G. Piazza, P. J. Stephanou, and A. P. Pisano, "One and two port piezoelectric higher order contour-mode MEMS resonators for mechanical signal processing," *Solid-State Electronics*, vol. 51, pp. 1596-1608, Nov-Dec 2007.
- [52] S. Strite and H. Morkoc, "GaN, AlN, and InN - a review," *Journal of Vacuum Science & Technology B*, vol. 10, pp. 1237-1266, Jul-Aug 1992.
- [53] H. O. Pierson, *Handbook of Refractory Carbides and Nitrides: Properties, Characteristics, Processing and Applications*, Noyes Publications, 1996.
- [54] W. J. Meng, *Properties of Group III Nitrides*, EMIS Datareviews Series, INSPEC, 1994.
- [55] K. M. Lakin, J. Belsick, J. F. McDonald, and K. T. McCarron, "Improved bulk wave resonator coupling coefficient for wide bandwidth filters," *2001 IEEE Ultrasonics Symposium. Proceedings. An International Symposium (Cat. No.01CH37263)*, 01 2001.
- [56] H. Campanella, *Acoustic Wave and Electromechanical Resonators: Concept to Key Applications*, Artech House, 2010.
- [57] K. M. Lakin, G. R. Kline, and K. T. McCarron, "High-Q microwave acoustic resonators and filters," *Ieee Transactions on Microwave Theory and Techniques*, vol. 41, pp. 2139-2146, Dec 1993.
- [58] Collaboration, "IEEE standard on piezoelectricity," Inst. Electr. & Electron. Eng., New York, NY, USA, Copyright 1988, IEE ANSI/IEEE Std 176-1987, 1988.
- [59] J. H. Kuypers and A. P. Pisano, "Interpolation Technique for Fast Analysis of Surface Acoustic Wave and Lamb Wave Devices," *Japanese Journal of Applied Physics*, vol. 48, Jul 2009.
- [60] R. Ruby, R. Parker, and D. Feld, "Method of extracting unloaded Q applied across different resonator technologies," *IEEE International Ultrasonics Symposium*, 2008.